UTRECHT UNIVERSITY

MASTER'S DEGREE THESIS

The effect of river network parameterization on large-scale flood modelling - a case study for the Amazon Basin

Author:
Jonathan Bänziger
Student ID: 5801117

Supervisors:
Dr. Rens van Beek
Jannis Hoch

in partial fulfillment of the requirements
for the degree of

Master of Science in Earth Surface and Water

December 8, 2017

Abstract

Flood events worldwide are likely to occur more frequently in the future as a result of a changing climate. Inundation models are thus an important tool to understand, assess and predict both flood events and their impacts. For 1D/2D model schemes, the drainage network and bathymetry of the river are essential inputs. Various river network densities and bathymetry schematizations are likely to affect the results of flood inundation models. The river drainage network determines flow path lengths and hence travel times. River bathymetry defines whether overland flow may occur and has also a determining influence on the channel friction because it affects water depths. In this study, the effect of different river network extents and bathymetry parameterizations on the simulation of discharge, water level, and inundation extent was investigated by performing a sensitivity and accuracy analysis. In addition, run times due to different 1D channel network densities were compared to investigate the trade-off between computational costs and output yield. The hydrodynamic model Delft3D Flexible Mesh (FM) was applied for the Amazon River basin. By means of a synthetic test case, Delft3D FM ran standalone for the sensitivity analysis. For the accuracy analysis, Delft3D FM was one-directionally and spatially coupled to the hydrological model PCR-GLOBWB, which provided daily water inputs to Delft3D FM. The agreement between simulated discharge, water level, and inundation extent was subsequently validated against observations.

The sensitivity analysis shows that in case of dry initial conditions in the 1D/2D domain, both 1D network and river bathymetry impact simulated discharge and water levels. A higher 1D network density accumulates and conveys more water downstream, causing also a higher peak discharge compared with a sparser network. In addition, it results in a faster hydrologic response since water in the channel flows at a higher rate than on the floodplain. Validating modelled discharge results shows that during low water the impact of the 1D channel network dominates over river bathymetry, whereas during high water river bathymetry was found to be dominant. River bathymetry derived from remote sensing techniques on a sparser network leads overall to the best model performance regarding Kling-Gupta efficiency (KGE) in which computational costs are minimized as well. During low and high water, however, the applied validation measures vary considerably among the bathymetry parameterizations indicating that river bathymetry has a profound effect on simulated discharge. Inundation extent was found to vary with both 1D network extent and river bathymetry, although the applied validation measures indicate similar scores. We identified that water on the floodplain of the Amazon River is not able to drain, hence leading to a consistently inundated floodplain which possibly hampers the potential effect of the different river network schematizations on the simulation of discharge, water level, and inundation extent. This issue needs to be addressed in future studies, for instance, by including a river bifurcation scheme allowing the enormous water volumes occurring in the river delta to be allocated over multiple river branches.

Acknowledgements

I would like to express my sincere gratitude to my first supervisor dr. Rens van Beek who gave me the opportunity to do this MSc research project in the field of large-scale inundation modelling. I thank him for providing insightful comments and suggestions during the entire research process. Especially his advice and comments to scientific related questions have been a great help. Moreover, I owe my deepest gratitude to Jannis Hoch who shared his knowledge and let me profit from his practical experience. He helped me with all my seemingly endless questions regarding the hydrodynamic model Delft3D Flexible Mesh and the model coupling to the hydrological model PCR-GLOBWB. For that I am very grateful. Without him, this work would not have been possible.

My thanks goes further to Hessel Winsemius and Herman Kernkamp from Deltares for their advice and support with Delft3D Flexible Mesh. Deltares provided me with a working laptop and access to their facilities and servers. Last but not least, I wish to thank my parents Annamarie and Werner for their continuous support during this research process but also during my entire study time. Thank you.

Contents

List of Figures

List of Tables

Chapter 1

Introduction

1.1 Large-scale flood modelling

1.1.1 The relevance of large-scale flood modelling

In many parts of the world, flooding is the leading cause of losses from natural phenomena accounting to more than US$ 250 billion damage worldwide over the period 1995-2005 (Kron, 2005). Floods also claimed about 100,000 human lives and affected over 1.4 billion people in the last decade of the 20th century (Jonkman, 2005). On-going climate change, intensified urbanization and land use changes amplify flood risks globally and thus modelling flood hazard and risk take on greater significance (Hollis, 1975; Bradshaw et al., 2007; Hirabayashi et al., 2013). Flood risk assessments are carried out at any spatial scale depending on the area of interest, ranging from micro-scale (e.g. effects of flooding on critical infrastructures) to larger scales such as national, continental, or even global scales (e.g. total effects of catastrophic flooding for a country). From a modelling point of view, flood waves show strong spatial correlation between neighbouring river basins which therefore evokes the need for large-scale modelling approaches (Jongman et al., 2014). It is also the major scale for evaluating how water resources will be influenced by e.g. climate change and variability (Paz et al., 2011). In addition, national risk policies, large-scale disaster management planning, and the (re-)insurance sector rely on large-scale risk assessments and hence large-scale models (de Moel et al., 2015; Falter et al., 2016). Thus, in the last few years, various flood inundation models have been developed to understand, assess, and predict both flood events and their impacts (Teng et al., 2017). The simulation of flood wave propagation and attenuation, water level and flood extent is crucial to denote flood hazard. The propagation and timing of the flood wave for instance is critical for evacuation planning whereas water level is a main factor to assess flood damage (de Moel et al., 2009).

1.1.2 Large-scale flood modelling in the Amazon Basin

The Amazon Basin has experienced several flood and drought events during the last decades whereby these extreme climate events are often driven by ENSO (El Niño-Southern Oscillation) episodes in the tropical Pacific (Chen et al., 2010; Marengo and Espinoza, 2016) and are likely to occur more frequently in the future due to climate change. The Amazon flood wave is known to be diffusive and subcritical in its characteristic (Trigg et al., 2009) and hence facilitates backwater effects which in turn are crucial flood-triggering processes in the Amazon Basin (Meade et al., 1991; Paiva et al., 2013b). To capture these flow characteristics, a hydrodynamic model is needed. There are three commonly used schemes for hydrodynamic river modelling which are: i) 1D, ii) 2D, and iii) 1D/2D models

(Figure 1.1). One-dimensional (1D) models describe the river channel as a series of cross sections perpendicular to the flow direction, and employ the Saint Venant equations based on conservation of mass and momentum equations for flow routing at these cross sections. Floodplain is either considered as storage areas or extended cross sections are used to represent both main channel and floodplain. By interpolating cross sections of water level and using a digital elevation model, 2D inundation maps can be derived (Paz et al., 2011). 1D models lack to simulate the lateral water exchange between the channel and the floodplain as well as floodplain flow which are both important processes especially in flat river systems with large floodplains like the Amazon (Alsdorf et al., 2010; Trigg et al., 2012; Yamazaki et al., 2012a; Paiva et al., 2013a). 2D schemes solve the Saint Venant equations two-dimensionally on a grid or mesh, representing river hydraulics which are more consistent with known processes (Bates and De Roo, 2000). However, 2D river flow modelling requires a precise meshing of the river bed in order to correctly take the topography into account which in turn results in increased computational cost (Finaud-Guyot et al., 2011). Especially for large-scale model applications, using a complete 2D river scheme may be not suitable due to excessive computational costs, and limited bathymetric data availability (Smith et al., 2006; Legleiter and Kyriakidis, 2008; de Moel et al., 2015; Falter et al., 2016). More recent modelling approaches employ a 1D model for simulating the hydrologic regime of rivers and a 2D model for simulating the inundation and flow on the floodplains (Paz et al., 2011; Falter et al., 2016). The present study simulates the Amazon flood wave, that is flood wave propagation and attenuation, water level, and flood extent, by means of such a 1D/2D model scheme. The large-scale model domain covers an area of around 1.2 x 10^6 km^2 which is a fifth of the entire Amazon Basin.

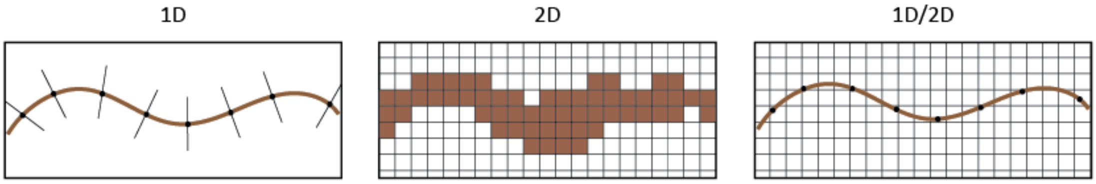

Figure 1.1: Commonly used schemes in hydrodynamic modelling; 1D, 2D, 1D/2D.

1.1.3 The crux of river network parameterization

1D/2D model schemes require topographic data of the channel and the floodplain to act as model bathymetry (Mason et al., 2010). 1D channel representations assume typically rectangular channel geometry and hence bathymetric data such as river width and depth along the river channel is needed. Especially for large-scale applications, the acquisition of river bathymetry is not straightforward. Besides, only a few approaches have been proposed which derive bathymetric information from remote sensing techniques (Pavelsky and Smith, 2008; Yamazaki et al., 2014a) and from empirical relationships which link river bathymetry to either upstream area (Coe et al., 2008; Paiva et al., 2011b) or discharge (Moody and Troutman, 2002; Getirana et al., 2012). River bathymetry is known to play a crucial role in modelling flow hydrodynamics (Merwade et al., 2008; Merwade, 2009) and that variations in river bathymetry affect the simulation of discharge, water depth and inundation extent (Yamazaki et al., 2012b; Paiva et al., 2013a). River bathymetry defines whether inundation may occur and hence plays an essential role in regulating flood extents (Getirana et al., 2012). Since inundation in upstream areas attenuates and delays peak discharge in downstream areas, river bathymetry is likely to impact the hydrologic response in a watershed in terms flood wave propagation and attenuation, and water stages as well. Moreover, channel friction is most pronounced at the bottom and the walls of the river which in turn is defined by the river bathymetry. If the friction influence is larger, this may cause water to be stored in the channel rather than being discharged. All aforementioned parameterization strategies are commonly used in large-scale inundation modelling but no study so far evaluated how different bathymetry parameterizations may influence the hydrodynamic simulation of floods. The present study explores the role of river bathymetry resulting from different parameterization strategies in terms of model sensitivity and accuracy. It is expected that river bathymetry derived from remote sensing depicts local conditions more accurately than when obtained by a simple empirical relationship.

For large, flat river systems where floodplains play an important role, the existence of small channels which ensure floodplain connectivity is crucial and improve simulation accuracy in terms of water level simulation, wave propagation speed, and inundation extent (Neal et al., 2012; Trigg et al., 2012). For the 1D/2D model scheme, a distinction of the model domain between the channel (1D) and the floodplain (2D) has to be made. Channel and floodplain exhibit different roughness coefficients in which the latter is typically larger (Mason et al., 2010). The channel network extent thus might influence the hydrologic response since water is able to flow at a higher rate within the channels. There is still a lack of knowledge to what extent model sensitivity and accuracy, in terms of flood simulation, are reliant upon the river network extent. In addition, different river network densities come with a different amount of computational nodes which will translate in increased computational costs in case of a higher channel density. Therefore, it is important to understand the role of different network densities on the simulation of floods. If the model results are insensitive to the river network, a sparser river network could be used to minimize computational costs which is an important economical aspect.

1.2 Research objective and research questions

The present research project applies a 1D/2D hydrodynamic model to simulate river discharge (i.e. flood wave propagation and attenuation), water level, and inundation extent. The study aims at gaining new insights into the role of the 1D channel network density and bathymetric input for large-scale hydrodynamic simulations of floods. This impact is explored by performing both a sensitivity and an accuracy analysis. By means of a synthetic test case, the former identifies to what extent different 1D channel network densities and river bathymetries (henceforth referred to as schematizations) affect the model results. The latter investigates the agreement between the model outcomes resulting from the different schematizations and observations. The Amazon Basin is used as test side.

This work aims to answer five research questions:

1. How sensitive is the model to different 1D channel network densities in terms of overbank storage and the consequent flood wave propagation and attenuation?
2. How sensitive is the model to varying river bathymetries, originating from different parameterization strategies, in terms of overbank storage and the consequent flood wave propagation and attenuation?
3. Which 1D channel network density results in the most accurate model performance with regard to river discharge, water level, and inundation extent when compared with in-situ measurements and remote sensing observations, respectively?

4. Which parameterization strategy, used to derive river bathymetry, results in the most accurate model performance with regard to river discharge, water level, and inundation extent when compared with in-situ measurements and remote sensing observations, respectively?
5. Is there a possible trade-off between computational costs and model accuracy in terms of discharge, water level, and inundation extent?

1.3 Approach

To simulate the Amazon flood wave, the state-of-the-art hydrodynamic model Delft3D Flexible Mesh (FM) (Kernkamp et al., 2011; Deltares, 2016) is used. The sensitivity and accuracy analyses are performed using four different 1D channel network densities and four different bathymetry parameterizations. River bathymetry was derived based on empirical relationships which link bathymetry to either discharge (Getirana et al., 2012), or upstream area (Paiva et al., 2011b), and satellite imagery (Yamazaki et al., 2014a). Delft3D FM rely on boundary influxes which can be set up in two ways; throughout model internal boundary conditions or a coupled model framework in which the output from another numerical model is used as input to Delft3D FM. To exclude any external bias and uncertainty influences introduced by e.g. such a coupled model framework, Delft3D FM run standalone for the sensitivity analysis. This means that model internal boundary conditions were used to supply Delft3D FM with water. The model outcomes from the schematizations are validated against observations in the accuracy analysis. This requires that the boundary conditions are based on observational data in order to reproduce a real world scenario. Discharge boundary conditions might be derived for instance from observation stations which in turn makes the model highly dependent on the availability and location of these stations (Hoch et al., 2017a). Important spatially distributed rainfall events might not be captured by the stations. Due to the lack of simulating significant processes such as evapotranspiration, infiltration, soil water storage, groundwater storage, or canopy interception in Delft3D FM, using rainfall boundary conditions will consequently cause all incoming precipitation to be discharged. This, however, would not represent the Amazon hydrology in a realistic manner. Therefore, in order to supply water to the hydrodynamic model, Delft3D FM is coupled to the hydrological model PCR-GLOBWB (van Beek and Bierkens, 2009) as done by Hoch et al. (2017a). The authors used a one-directional and spatially explicit coupling approach between the large-scale hydrological model PCR-GLOBWB and Delft3D FM.

1.4 Thesis outline

The thesis firstly provides a brief literature review about the state of the art in the area of flood inundation modelling and how various model structures, input data, and parameterizations affect the simulation of floods (Chapter 2). The study area in the Amazon Basin is then described in Chapter 3. Afterwards, the river network parameterizations as well as the methods for the respective sensitivity and accuracy analysis are outlined in Chapter 4. The results for both sensitivity and accuracy analysis are provided in Chapter 5. Chapter 6 discusses subsequently the obtained results. The conclusions are drawn in Chapter 7 and final recommendations given in Chapter 8.

Chapter 2

Literature review

There are many ways to set up a flood inundation model. During the modelling process, modellers have to make various choices and assumptions such as: i) the processes to be modelled, ii) the mathematical representation of these processes, iii) the spatial and temporal scale and resolution on which the processes will be modelled, iv) the model's parameters, and v) the model's input data (Guswa et al., 2014). The choices made can have a considerable impact on the resultant model performance and accuracy. How differences in e.g. the mathematical representation of certain processes, the model structure, parameterization or input data affect the simulation of floods has been investigated in many studies. On the one hand, such studies provide crucial understanding of how to improve the general performance of flood inundation simulations and, on the other hand, how to facilitate the decision-making process if setting up a new model. The present study tries to contribute to the valuable information gained from such studies by investigating the effect of river network parameterization on large-scale flood modelling.

2.1 Model schemes

2.1.1 1D, 2D, and 1D/2D

Horritt and Bates (2002) evaluated a 1D, 2D and 1D/2D numerical model for predicting river flood inundation on a 60 km reach of the river Severn, UK. The study revealed that the 1D/2D and 2D model are capable of making equally good predictions of inundated area. Apel et al. (2009) also compared models of different complexities for a case study in Germany. The authors concluded that the 2D and 1D/2D model gave the best overall model performances with good matches to the surveyed inundation depths and extent. However, they also highlighted the drawback of the 2D hydrodynamic model in terms of long run times and concluded that the 1D/2D model provides the best compromise between data requirements, simulation effort, and acceptable accuracy of the results. For large-scale applications where a fully 2D model scheme is almost not feasible due to computational constraints and limited data availability, a 1D/2D model scheme is preferable. According to Hoch et al. (2017a), it also yields a better spatial resolution of the river network than the 2D scheme which is more dependent on the quality and resolution of the digital elevation model (DEM). Depending on the study site, Neal et al. (2012) found that models neglecting either the channels or the floodplain lacked any predictive skill. For large, flat river systems, a channel and floodplain component are both necessary to accurately simulate the hydraulics.

2.2 Model structure

2.2.1 Model resolution

The model structure (i.e. process description, coupling of processes, numerical discretization or spatial resolution) is known to strongly impact the model performance (Butts et al., 2004). Horritt and Bates (2001) tested how different spatial model resolutions ranging from 1,000 m to 10 m (pixel size) performed in terms of predicted inundated area and flood wave travel times. The authors showed that predicted flood wave travel times are strongly dependent on the model resolution. Inundation extent, in turn, was constant with respect to changes in scale. Another study carried out by Horritt et al. (2006) stated that their model showed greater sensitivity to mesh (grid) resolution than topographic sampling. Their model resolutions ranged from 2.5 m to 50 m. The model's spatial resolution is, however, restricted to the computational costs. For large-scale model applications, the existing trade-off between model resolution and computational costs consequently results in the usage of coarser grids (meshes) and hence in greater losses of topographic information. A finer spatial model resolution is able to comprise more topographic details but leads to more model grid elements and requires also smaller model time steps which in turn increases computational costs. Furthermore, the flood pulse may well travel for months over a large model domain which then also requires a certain minimum of simulation time (Paz et al., 2011).

2.2.2 River drainage network

River networks are mainly extracted from digital elevation models based on the procedure proposed by O'Callaghan and Mark (1984). This automated procedure includes first the creation of a drainage direction matrix as well as a pit removal. Secondly, a drainage accumulation matrix is generated. River channels are then obtained by defining all points with accumulated drainage areas above some threshold (O'Callaghan and Mark, 1984). The river network density is thus controlled by the threshold criterion of accumulation area. The threshold ideally represents the critical accumulation area where runoff is sufficiently concentrated and fluvial processes dominant (O'Callaghan and Mark, 1984). Tarboton et al. (1991) emphasize the relevance of this threshold and suggest that the extracted drainage network should have a resolution as high as possible and "be close to what traditional workers using maps or fieldwork would regard as channel networks" (Tarboton et al., 1991, p. 84). To date, many researchers investigated and explored various ways to extract river networks from digital elevation models, for instance by applying several drainage direction algorithms (see e.g. Zhao et al., 2009) and pit removal techniques (see e.g. Poggio and Soille, 2012).

2.3 Model input data

2.3.1 DEM

The geometric description of the floodplains and sometimes of the river channels as well is derived from DEMs. The quality (accuracy) and resolution (precision) vary considerably among available DEMs and affect the model output performance when used as input to hydrodynamic modelling (Ali et al., 2015). Casas et al. (2006) compared the effects of DEMs derived from GPS, LiDAR, and vectorial cartography on hydrodynamic modelling of floods. Regarding the estimation of water level and inundated area of the floodplain, the contour-based DEM input resulted in the least accurate estimate whereas the LiDAR-based DEM input showed the highest accuracy. LiDAR-DEMs are known to exhibit very high spatial resolution and great vertical accuracy. However, the acquisition on large scales is very costly and is limited in wetland areas as well as under cloudy and rainy conditions (Schumann et al., 2016). Contour mapping may also not be favourable for large scales as it is time consuming and may not be possible for some remote areas (Ali et al., 2015). Low-cost DEMs such as SRTM (Shuttle Radar Topography Mission) are globally available but have a coarse spatial resolution (around 30 m to 90 m, Farr et al., 2007) and a coarse vertical resolution (average absolute height error of around 6 m to 7 m globally, Rodríguez et al., 2005). Schumann et al. (2008) compared water stages and inundation area derived from three different DEM sources (LiDAR, topographic contours, and SRTM). The LiDAR input resulted in the best performance followed by the contour DEM and SRTM. Despite having a low vertical precision, SRTM performed relatively good and the authors suggested that for large, homogeneous floodplains SRTM is a valuable source of information. Yan et al. (2013) explored the potential of SRTM topographic data for flood inundation modelling by comparing a hydraulic model based on high-quality topography (LiDAR) and one based on SRTM topography. The results showed, despite significant differences between the two topography models, an accuracy that is typical for large-scale flood studies (Yan et al. 2013). Ali et al. (2015) mentioned also the importance of the DEMs accuracy over the DEMs resolution. The authors resampled the high resolution LiDAR DEM to the same resolution (90 m) than the SRTM DEM and compared then the performances of a 1D hydraulic model using both inputs. The model based on the 90 m DEM derived from the resampled LiDAR performed better than the model based on the 90 m DEM derived from SRTM. Besides the lower accuracy and precision of available DEMs on larger scales, the possibility to describe the geometry of the floodplains and river channels in great detail for large-scale model applications is also severely limited by the aforementioned resolution of the computational grid or mesh of the hydrodynamic model.

2.3.2 Hydrology

Flood inundation models require discharge data to provide model boundary conditions (Mason et al., 2010). As mentioned in Chapter 1.3, deriving upstream boundary conditions from observation stations makes the hydrodynamic model highly dependent on the presence and spacing of the stations (Hoch et al., 2017a). Pappenberger et al. (2006) also found that uncertainty of upstream boundary can have significant impact on the model results. Besides, hydrodynamic models are forced with synthetic storm events of varying return periods to derive for instance flood inundation maps for extreme storm events (Ghimire, 2013). Rather than being measured, input flow rates can also be predicted by a hydrological model and added to the hydrodynamic model throughout a coupled model framework. Large-scale hydrological models such as VIC (Liang et al., 1994), PCR-GLOBWB (van Beek and Bierkens, 2009), and SWAT (Arnold et al., 2012) describe the terrestrial water cycle and try to represent the role of different soil and vegetation types on the streamflow generation processes and on water and energy budgets of the basin (Paiva et al., 2011b). Based on the water balance equation and hence by considering processes such as evapotranspiration, infiltration, percolation, and soil and groundwater storage interactions, these hydrological models are capable of simulating available runoff volumes. In the last few years, inundation modelling has begun to integrate both hydrological and hydrodynamic models. That is lateral inflows to a river network from e.g. rainfall which occurred in the catchment area are calculated by a hydrological model, whereas afterwards the propagation of the flood wave along the river reach is simulated by a hydrodynamic model (Biancamaria et al., 2009; Bravo et al., 2011; Paiva et al., 2011b; Schumann et al., 2013; Amir et al., 2015). Hoch et al. (2017a) assessed, among others, the model performance when the hydrodynamic model Delft3D FM was forced with upstream discharge boundary conditions as well as when Delft3D FM was spatially coupled with the hydrological model PCR-GLOBWB. The results yielded that inundation cannot be simulated if the river reach is not fed by upstream discharge boundaries and that the peak flow is better captured by the coupled framework than by forcing Delft3D FM with discharge boundary conditions. Coupling hydrology and hydrodynamics has been shown to provide a more coherent and comprehensive description of runoff phenomena and flow characteristics (Kim et al., 2012) and hence might improve flood hazard and risk assessments. The subsequent Chapter 2.3.2.1 gives a brief description of the hydrological model PCR-GLOBWB applied in the present study.

2.3.2.1 The hydrological model PCR-GLOBWB

PCR-GLOBWB, short for PCRaster GLOBal Water Balance (hereinafter termed PCR), is a grid-based model written in PCRaster (Wesseling et al., 1996) which describes the global terrestrial water cycle (van Beek and Bierkens, 2009). The current resolution is 30 arcmin which is approximately 55 km x 55 km at the Equator. The model differentiates between two vertically stacked soil layers, an underlying groundwater layer and a surface canopy layer. Water storage is calculated for each of these aforementioned compartments on a cell-by-cell basis and for each daily time step. Water can exchange between the layers (percolation, capillary rise) and between the top layer and the atmosphere (rainfall, evaporation and snowmelt). In addition to the canopy interception, the model is also able to simulate snow storage (van Beek and Bierkens, 2009). Vertical water fluxes between the lower soil reservoir and the groundwater reservoir are mainly downwards but capillary rise may force the water to enter the soil reservoir during periods of low soil moisture contents (Wada et al., 2010). Water can leave a cell laterally as overland flow (QDR), interflow (QSf) and baseflow (QBf), as indicated in Figure 2.1, and may finally end up in the river channel (QChannel) where specific runoff is routed along a local drainage direction (LDD) network. Routing of surface water flow is based on the kinematic wave approximation of the Saint-Venant Equation and includes evaporative losses from lakes, reservoirs and floodplains (van Beek and Bierkens, 2009). In addition, advanced schemes for subgrid parameterization of surface runoff, interflow and baseflow are implemented which consider separately tall and short vegetation, open water, different soil types, fractional area of saturated soil, and frequency distribution of groundwater depth based on surface elevations (van Beek et al., 2012).

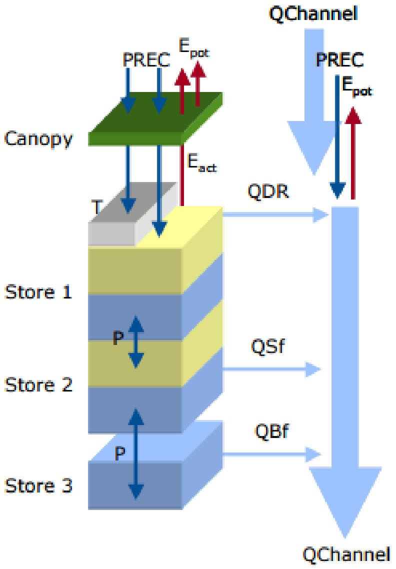

Figure 2.1: Scheme of the four vertically stacked, interactive layers representing canopy, soil, and groundwater in PCR (van Beek and Bierkens, 2009).

PCR can be forced with observed global climate data (e.g. Climate Research Unit) or with simulated precipitation and evaporation from climate models (e.g. GCM). Alternatively, the model is also able to calculate actual evaporation from potential evaporation and soil moisture status based on Penman-Monteith (van Beek and Bierkens, 2009). The model provides also an option to include human water use such for irrigation, households and industry (Wada et al., 2016). Various studies applied PCR for instance to simulate global freshwater surface temperatures (van Beek et al., 2012), global water stress (van Beek et al., 2011), and global depletion of groundwater resources (Wada et al., 2010), to assess global river flood risk (Winsemius et al., 2013), to provide inputs of recharge and surface water levels for groundwater models (Sutanudjaja et al., 2014; de Graaf et al., 2015), or to model global water use (Wada et al., 2014, 2016).

2.4 Model parameterization

2.4.1 Friction coefficient

The channel and floodplain roughness coefficients are considered to be sensitive model parameters. Paiva et al. (2013a) and Yamazaki et al. (2011) showed that changes in the channel friction affected simulated discharge, flooded area, and water depth. The channel friction value is often determined throughout a calibration procedure (Horritt and Bates, 2001; Trigg et al., 2009; Rudorff et al., 2014). For 1D/2D model applications where the floodplain flow is also taken into account, a floodplain friction is required. Different vegetation types such as forest or grassy landscape are represented by different friction values. Rudorff et al. (2014) emphasized the importance of spatially varying floodplain frictions as heterogeneous, distributed floodplain vegetation makes the use of a single floodplain friction value inappropriate. In addition, using spatially variable floodplain frictions resulted in a lower model sensitivity than compared with a constant, single floodplain coefficient (Werner et al., 2005). A variable-floodplain-friction model makes it possible to use different input data to predict flood extents for different flood events whereas a constant-floodplain-friction model would then require a recalibration (Mason et al., 2003).

Horritt and Bates (2002) evaluated the effect of different channel and floodplain frictions on flood inundation. They showed that the sensitivity of floodplain friction is minimal when the channel friction is low. A low channel friction leads to low water levels which in turn causes little inundation. If the channel friction is high, water depth in the channel is increased and hence more water is spilled onto the floodplain. As a result, the floodplain friction takes on greater significance regarding its influence on travel times and inundation extents (Horritt and Bates, 2002). However, it should be noted that different hydrodynamic models respond differently to changes in channel and floodplain frictions (Horritt and Bates, 2002).

2.4.2 River bathymetry

River bathymetry is commonly represented one- or two-dimensionally and depending on which model scheme (Figure 1.1) is used, different methods exist to derive this bathymetric information. 2D hydrodynamic models, for instance, require detailed channel topography. High resolution sonar (Horritt et al., 2006), airborne LiDAR (Hilldale and Raff, 2008), remote sensing imaging (Legleiter and Roberts, 2009), and traditional survey and GPS are a few methods to name. Traditional survey and GPS are limited to wadeable river stream conditions and are not favourable on larger scales. Sonar data cannot be acquired in shallow waters, whereas LiDAR does not work well in deep waters. Moreover, sonar and LiDAR are both expensive methods (Conner and Tonina, 2014). Another technique is to collect cross-section data with traditional survey or sonar equipment and interpolate a channel surface between the cross-sections (Merwade et al., 2008; Conner and Tonina, 2014). However, for large-scale model applications where a fully 2D model scheme is not possible due to computational constraints, a 1D/2D model is usually used.

Chapter 3

Study area

3.1 Geography of the Amazon Basin

Surrounded by the mountain range of the Andes in the west, the Guianas massif in the north, and the Central Brazil massif in the south, the Amazon Basin comprises a drainage area of around 6 x 10^6 km^2 (Salati and Vose, 1984). In the middle of these high elevation border zones lie the vast Amazonian lowlands which are open to the east where the Amazon River empties into the Atlantic. The entire river system is located in the tropics and around 5 x 10^6 km^2 of the Amazon Basin is covered by high tropical rainforest (Sioli, 1984). Regarding the Brazilian naming, the mainstem river is called Solimoes River until the confluence with the Negro River at Manaus, after which it is called the Amazon River. With respect to the average discharge of around 200,000 m^3 s^{-1} at its mouth, the Amazon River is the world's largest river (Meade et al., 1991). In terms of river length, the Nile (6,671 km) is slightly longer than the Solimoes-Amazon main river (6,518 km). The river widths and depths of the Solimoes-Amazon, however, are incomparable with any other rivers where widths range on average from 4 km to 5 km and depths from 40 m and 50 m (Sioli, 1984). The Amazonian lowlands compose a river system with minimal river slopes and large floodplains. The river level at low-water season for instance at the mouth of the Negro River, 1,500 km from the sea, is only about 15 m above sea level (Sioli, 1984). Likewise in the low-water season, the physical influence of sea tides can be felt more than 1,000 km upstream from the sea (Sioli, 1984; Kosuth et al., 2009). The vast floodplains in the middle and lower Amazon are annually flooded for several months (Sioli, 1984) and play an important role in terms of dampening discharge extremes in the Solimoes-Amazon River mainstem due to seasonal water storage on the floodplain (Meade et al., 1991). The floodplains further impact large-scale flood propagation (Paiva et al., 2011a; Yamazaki et al., 2011), and play a significant role in biological and biochemical processes (Trigg et al., 2009), sediment dynamics, and chemical and ecological conditions (Paiva et al., 2013a).

3.2 Climatology of the Amazon Basin

The average annual rainfall of the Amazon Basin is about 2,300 mm (Sioli, 1984; Bonell et al., 2005). Together with the great extent of drainage area it generates enormous water volumes. Being situated at the Equator, the Amazon Basin receives at its upper limit of the atmosphere a solar radiation of around 354-429 Watt/m^2 (Salati and Marques, 1984). The portion which reaches the ground is considerably less though. This is due to the high humidity and cloudiness which causes absorption and reflection of incoming solar radiation in the troposphere. The solar energy reaching the ground is then mainly driving evaporation processes, leaving only 30% of the energy for sensible heat flux. This gives the Amazon Basin an isothermic characteristic where monthly mean temperatures range from 24 °C to 28 °C with an annual variation of around 5 °C (Salati and Marques, 1984; Bonell et al., 2005). Around 55% of precipitation in the basin is evaporated or transpired by the forest and the remaining 45% is drained by the Amazon River (Salati and Marques, 1984). Extreme climate events such as floods and droughts are often driven by ENSO (El Niño-Southern Oscillation) episodes in the tropical Pacific or sea surface temperature (SST) anomalies in the tropical Atlantic and are thus likely to occur more frequently and severely with a warmer climate (Marengo et al., 2011). Additionally, humans have impacted the Amazonian ecosystem for centuries by deforestation and establishing grass or soy plantations. These human actions might well impact the hydrological cycle due to the changes in vegetation (Marengo et al., 2011). Deforestation leads to higher amounts of available runoff and increased temperatures as evapotranspiration and interception are reduced.

3.3 Model domain

The still relatively unaffected river basin in terms of man-made structures (Constantine et al., 2014), together with the occurrence of seasonal flooding (Sioli, 1984; Coe et al., 2002) makes the Amazon a widely used research object in the field of inundation modelling. The study area covers an area of around 1.2 x 10^6 km^2 which is a fifth of the entire Amazon Basin and is located in the Amazonian lowlands in Central Brazil (Figure 3.1). This area includes among other the river reaches from the Negro River in the north, Solimoes in the west, and Madeira in the south as well as the Amazon River itself up to its mouth in the east.

Figure 3.1: The study area is situated in the Amazonian lowlands and represents a fifth of the entire Amazon Basin.

Chapter 4

Methods

4.1 Delft3D Flexible Mesh

The integrated modeling suite Delft3D Flexible Mesh, developed by Deltares, provides a state-of-the-art model, D-FLOW Flexible Mesh (hereinafter termed DFM), for hydrodynamic calculations (Kernkamp et al., 2011). Non-steady flow and transport phenomena can be simulated in either one, two, or three dimensions. The flexible mesh allows the combination of rectilinear or curvilinear grids and unstructured grids composed of triangles, quads, pentagons, and hexagons (Deltares, 2016). Owing to this flexible discretization of the model domain, a finer grid can be implemented where high accuracy in the process description is needed (e.g. meandering river), while a coarser grid in areas where processes spatially less vary (e.g. a large, flat floodplain area) can be used to reduce runtime (Castro Gama et al., 2013). Unstructured grids also minimize discretization errors which are introduced by curved features such as boundaries of a river, an estuary or a coastal sea on structured grids (Deltares, 2016). DFM has been shown to be an efficient solver for shallow water equations on unstructured grids for tidal propagation on the Continental Shelf (Kernkamp et al., 2011). Muis et al. (2016) used the Delft3D FM software to simulate storm surges and thus calculate extreme sea levels on a global scale which showed good agreement with observed sea levels. DFM was also applied for inundation modelling along the highly modified Yellow River in China (Castro Gama et al., 2013).

The system of equations consists of the equations of continuity (mass conservation) and motion (momentum conservation), and transport equations for conservative constituents (Deltares, 2016). In the two-dimensional mode, DFM solves the Reynolds-averaged Navier-Stokes equations (RANS) for an incompressible fluid, under the shallow water and the Boussinesq assumptions (Deltares, 2016). Hence, vertical momentum exchange is assumed to be negligible as well as that the vertical velocity component (z direction) is much smaller than the horizontal ones (x and y direction). In addition, pressure gain is assumed to be linear with depth which leads to a hydrostatic pressure distribution. This means that the three-dimensional RANS equations can be reduced to the two-dimensional so-called shallow water equations by averaging the RANS equations over depth. The Boussinesq assumption implies that density variability is a function of pressure only (Deltares, 2016). Conservation of mass and momentum are expressed in the shallow-water equations by (Kernkamp et al., 2011):

$$\frac{\partial H}{\partial t} + \nabla * (Hu) = q, \tag{4.1}$$

$$\frac{\partial u}{\partial t} + adv(u) + g\nabla\zeta + c_f u\|u\| + 2\Omega \times u = d, \tag{4.2}$$

where H denotes the total water depth, $\nabla \equiv [\partial_x, \partial_y]^T$ the horizontal gradient operator, u the depth-averaged horizontal velocity vector, $adv(u)$ the advection term, ζ the water level relative to a reference plane, and Ω the earth rotation vector. The constants g and c_f express the gravity constant and the bottom-friction coefficient, respectively. The right-hand side q contains source terms and d contains external forcing.

The set of equations are formulated in orthogonal curvilinear coordinates or in spherical coordinates (Deltares, 2016). Orthogonality of the grid is a crucial condition to maintain an implicit time integration of the equations (Kramer and Stelling, 2008) and is, in addition, computationally efficient (Kernkamp et al., 2011). For the two-dimensional (depth-averaged) mode, only one computational layer exists which is represented by an unstructured, staggered grid in the horizontal plane. Unlike collocated grids, variables such as pressure and directional velocity components in a staggered grid are defined at different positions. This provides an efficient implicit solution technique (see further Stelling and Duinmeijer, 2003). Figure 4.1 illustrates how two grid sections of differently sized quadrangles can be connected via triangles. In addition, it shows the concept of staggered grids where pressure and velocity points are separately located. The pressure points are defined at the cell circumcentres, whereas the velocity points are on the cell faces (Figure 4.1). A grid is considered to be orthogonal if the flow link or line segment which connects two adjacent cell circumcentres intersects orthogonally with the interface between them. The pressure gradient for instance, hence, can be described by only two pressure points which is computationally efficient.

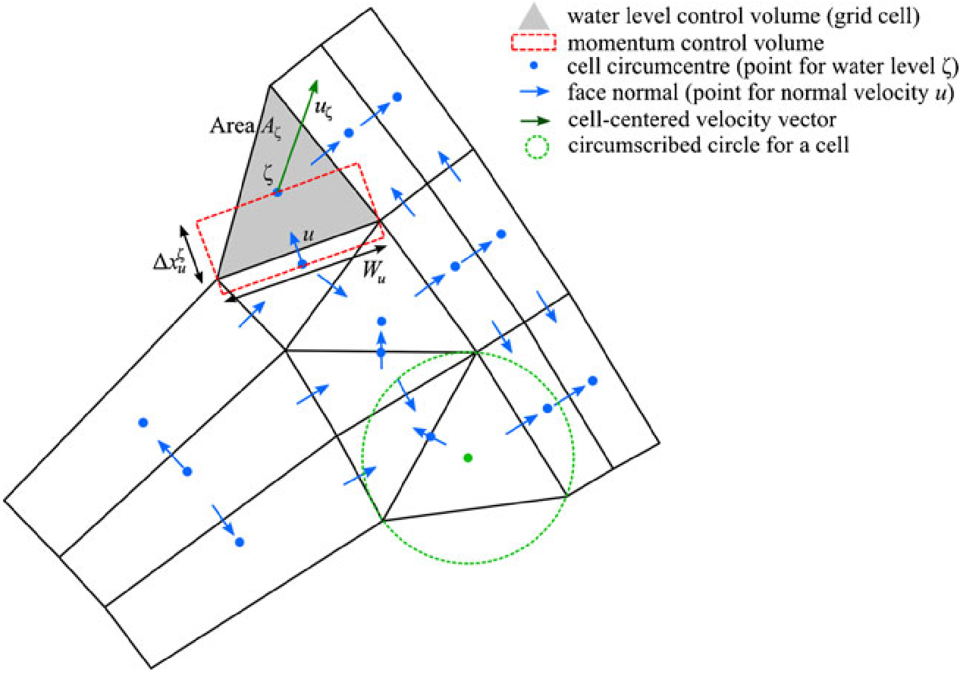

Figure 4.1: Unstructured grid of DFM with differently sized quadrangles and triangles. Principle of staggered grids where variables are separately located (Kernkamp et al., 2011).

DFM uses a finite volume discretization method where the continuity equation is solved implicitly for all points in a single combined system. However, the advection terms are treated explicitly with a time-step limitation based on the Courant criterion in order to ensure numerical stability (Deltares, 2016). The Courant number which is defined in one-dimension as $C = \frac{u * \Delta t}{\Delta x}$ provides a measure of how fast a quantity (e.g. a fluid) propagates through a grid cell within a given time step, where u denotes the velocity of the fluid under consideration, Δt the time step of the model, and Δx the size of the grid cell. Preferably, the quantity travels from one grid cell to its adjacent grid cell within the given time step. If the time step is too large and the quantity travels further within a time step, this would lead to missing information at the adjacent grid cell for the numerical calculations and might cause numerical instability. In order to ensure numerical stability, the Courant-Friedrichs-Lewy (CFL) condition (Courant et al., 1928) limits the aforementioned equation to 1 ($C <= 1$). Hence, implementing a finer resolution of the grid cells would require also smaller time steps (assuming velocity u remains unchanged) which in turn would lead to increased computational time. In DFM, the user can specify the maximum allowed Courant number and is advised to select a value of 0.7 or lower due to the explicit advection scheme used in DFM (Deltares, 2016). Based on the various sizes of the grid cells and the maximum allowed Courant number, DFM computes subsequently the time steps of the model. For further documentation on DFM, this paper refers to Kernkamp et al. (2011) and the DFM user manual (Deltares, 2016).

4.2 Model setup

4.2.1 Defining the model domain

The area in this study was limited to flood-prone areas since hydrodynamic computations still require significant computational power for multi-year simulations (Hoch et al., 2017a). This was achieved by applying the terrain descriptor height above nearest drainage (HAND) (Rennó et al., 2008). The HAND grid yields the relative vertical distance to the nearest drainage network and can be used to classify terrain according to its drainage potential. Only grid cells exhibiting HAND values less than or equal to 25 m were used to delineate the study area. Additionally, the study extent comprises the most downstream hydrological observation station at Obidos (Figure 3.1) which discharge data was used to validate the model.

4.2.2 Defining the 2D flexible mesh

The floodplain is represented by a 2D mesh composed of differently sized quadrangles and triangles. The flexible mesh was generated by automatic local grid refinement of a coarser regular grid based on the obtained HAND values (Hoch et al., 2017a). The flexible mesh has the finest spatial resolution of 1.3 km for areas with lowest HAND values such as water bodies and floodplains while areas with higher HAND values and thus areas further away from water bodies exhibit a coarser spatial resolution (up to 5.4 km). Such a coarse model resolution is inevitable at this spatial scale ($\sim$1.2 x 10^6 km^2) to maintain a reasonable computational effort. The 2D flexible mesh composed of differently sized grid cells is shown in Figure 4.2. The 2D mesh represents the floodplain and thus surface elevations have to be assigned to each 2D grid cell. This can be achieved by interpolating elevation values from a DEM to the flexible mesh of DFM. The surface elevations for the study area were derived from the SRTM DEM, having a raster resolution of 0.025°($\sim$1.5 km at the Equator). The vertical accuracy of DEMs emanating from SRTM is influenced by vegetation cover where dense forest canopy and high vegetation heights such as present in the Amazon Basin leads to diminished accuracy (Baugh et al., 2013). Hence, an absolute vertical SRTM error of around 22 m was found in the Amazon (Carabajal and Harding, 2006). This is due to the inability of the C-band radar signal to fully penetrate dense vegetation canopy which in turn generates an overelevated DEM. Such overelevated DEMs prevent the correct simulation of overbank inundation and is improved when vegetation heights are removed from the DEM (Baugh et al., 2013). For this study, vegetation cover was removed as proposed by Baugh et al. (2013).

4.2.3 Defining the 1D network

The centre line of the 1D river network was derived based on the GWD-LR algorithm by Yamazaki et al. (2014a). Figure 4.2 shows for a section in the study area the centre line of the 1D river network as well as the 1D computational cross section nodes along the centre line. The spacing between the 1D cross section nodes is 1.3 km which equals the smallest grid size of the 2D domain for optimal flux exchange. The 1D cross section nodes represent the locations where channel bathymetry is inserted into the model. Therefore, sample points were created along the 1D river centre line with a spacing of around 5 km which contained river width and bed elevation information. The procedure to assign the required river widths and bed elevations to the computational nodes in DFM is summarized as follows:

1. For each sample point,
    1.1. obtain river width and depth
    1.2. obtain surface elevation
    1.3. derive river bed elevation by subtracting river depth from surface elevation
    1.4. store river width and bed elevation
2. Load sample points into DFM and interpolate bathymetry to the computational cross section nodes.

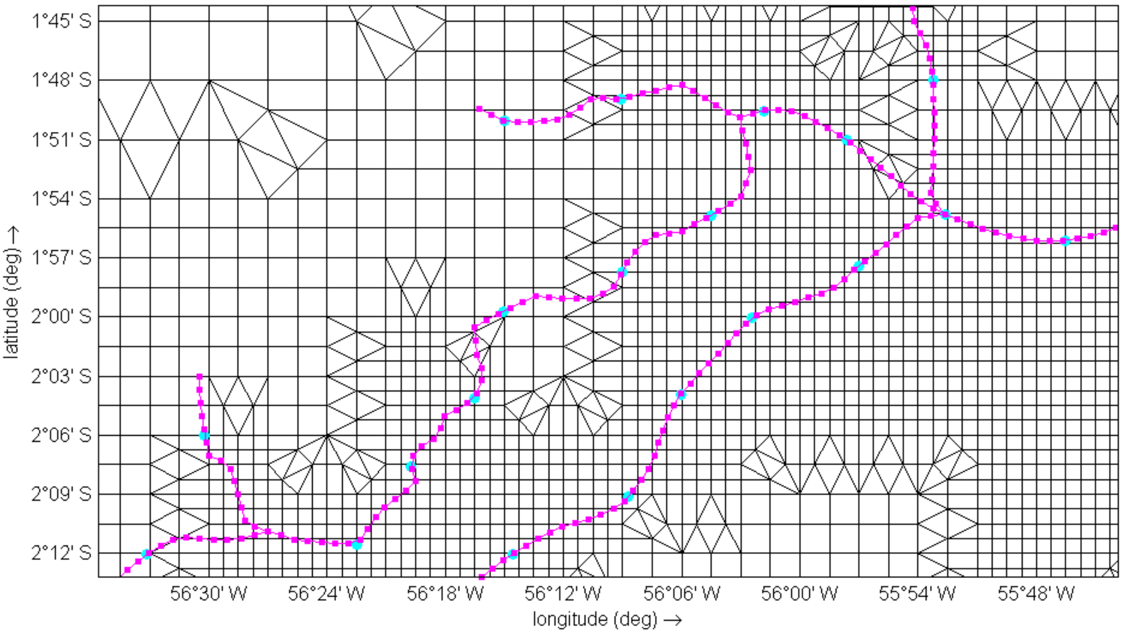

Figure 4.2: 2D floodplain mesh composed of quadrangles and triangles, 1D computational cross section nodes (magenta squares) and sample points (cyan dots) along the 1D network.

4.2.3.1 River network densities

River networks are usually derived from digital elevation models consisting of all cells with accumulated drainage area above a certain threshold (O'Callaghan and Mark, 1984). In the present study, four different thresholds of accumulation area were used to derive the 1D channel network densities: 10%, 1%, 0.1%, and 0.01% of the upstream area of the entire Amazon catchment (∼6 x 10^6 km^2). Figure 4.3 shows the resulting 1D channel network extents based on these four thresholds. The networks are henceforth referred to as **N10**, **N1**, **N01**, and **N001**. Typically, hydrological software applications such as Arc Hydro use a default threshold of 1% (see e.g. Dixon et al., 2015).

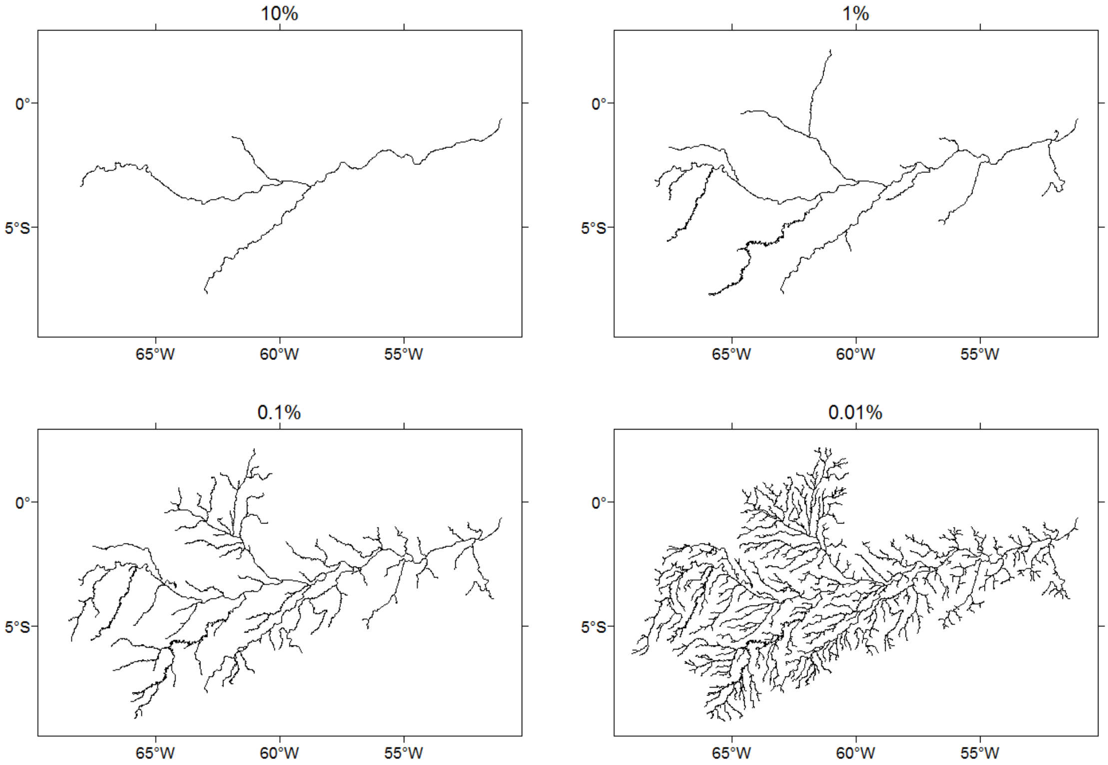

Figure 4.3: Resulting 1D channel network extents by using 10%, 1%, 0.1%, and 0.01% of accumulated drainage area as threshold.

4.2.3.2 River bathymetries

4.2.3.2.1 Parameterization strategies

River width and depth are essential first order parameters and have a profound effect on modelled discharge, inundation extent, and water depth (Yamazaki et al., 2012b; Paiva et al., 2013a). Leopold and Maddock (1953) linked river width and depth via power law relationships to discharge. This geomorphologic relationship between the hydraulic geometry and discharge has been widely used in literature (e.g. Moody and Troutman, 2002; Decharme et al., 2012). Based on the same relationship, Andreadis et al. (2013) derived a global river bankfull width and depth database. Besides discharge, river width and depth can also be connected via power law relationships to upstream area as done for instance by Coe et al. (2008) or Paiva et al. (2011b). More recent approaches derive river width from remotely sensed imagery (Pavelsky and Smith, 2008; Yamazaki et al., 2014a). River depth is afterwards obtained by using an empirical width-depth relation. For this study, four approaches were used to derive river width and depth information at the location of each sample point. Hereafter, these four approaches are named PS (Parameterization Strategy) followed by two letters defining the source (first letter from the authors which applied them originally) of river width and depth:

PS GG

Getirana et al. (2012) derived both river width and depth empirically from discharge by applying the subsequent power law relationships:

$$w = max(10, \beta Q^{0.5}), \tag{4.3}$$

$$d = max(2.0, \alpha w) \quad \alpha = 3.73 * 10^{-3}, \tag{4.4}$$

where w is river width [m], d denotes river depth [m], and Q is the annual mean discharge [m^3 s^{-1}]. The basin β coefficient for equatorial and subtropical basins is equal to 18 (Getirana et al. 2012). The raster resolution of available discharge data is often quite coarse (e.g. 1°in the hydrographic database from Cogley, 2003) which creates the problem that a single width and depth would be assigned to a large river segment and that smaller scale variability in width and depth is not taken into account. Additionally, all river channels within such a raster cell, being main stream or small tributaries, will have the same width and depth. This, of course, does not represent reality properly and therefore discharge was downscaled to a higher raster resolution by linking upstream drainage area to total runoff. To this end, PCR was used to simulate annual mean runoff over the period 1979 to 2001 (data from Weedon et al., 2014) at 5 arc min raster resolution. By multiplying annual mean runoff (m per year) with upstream drainage area (m^2) on a cell by cell basis, discharge at the same resolution (0.025°) of the upstream drainage area raster was obtained. At each sample point, the values of the underlying rasters, upstream drainage area and total runoff, were obtained and multiplied so as to derive discharge. River width and depth were then computed according to (4.3) and (4.4) and assigned to each sample point.

PS PP

Paiva et al. (2011b) derived river width and depth empirically from upstream drainage area. The authors used following geomorphologic equations for the Amazon River basin:

$$w = 0.8054 A_d^{0.52892}, \tag{4.5}$$

$$d = 1.4351 A_d^{0.1901}, \tag{4.6}$$

with A_d being the upstream area [km^2]. The coefficients of these two equations are based on cross section profiles from 341 gauge stations in the Brazilian part of the Amazon Basin (Paiva et al., 2011b). The same upstream drainage area raster is used as in the aforementioned discharge downscaling method applied in PS GG. Subsequently, the upstream drainage area at the location of each sample point along the river network was extracted and then linked via (4.5) and (4.6) to derive river width and depth.

PS YG

Yamazaki et al. (2014a) developed the global width database for large rivers (GWD-LR) and by linking the obtained river widths with the width-depth relation (4.4) from PS GG, river depth was retrieved. The GWD-LR database was used to extract the river width at the location of the sample points along the 1D channel network and river depths were subsequently assigned to them via the aforementioned width-depth relation. Yamazaki et al. (2014a) applied an algorithm which calculates river width from satellite-based water masks and flow direction maps. The GWD-LR database is based on the SRTM Water Body Data and the HydroSHEDS (Hydrological data and maps based on SHuttle Elevation Derivatives at multiple Scales) flow direction map. The SRTM Water Body Database itself is a by-product of the SRTM Digital Terrain Elevation Data where water bodies such as ocean, lakes or river shorelines were identified and delineated. The algorithm first fills island gaps in the water body mask, determines afterwards the river centerlines, generates then flow directions toward the centerlines and calculates finally the river width (see further details Yamazaki et al., 2014a). The HydroSHEDS flow direction map is used to ensure upstream-downstream connectivity along the river network in the water mask. It is worth noting that the SRTM Water Body Database is a snap shot of the water situation at the time of the shuttle flight in February 2000.

PS YP

Likewise PS YG, river width was derived from the GWD-LR database (Yamazaki et al., 2014a). The combination of the geomorphologic equations (4.5) and (4.6) from Paiva et al. (2011b) reveals the following width-depth relation:

$$d = 1.55w^{0.36}. \tag{4.7}$$

River depths were then acquired by inserting the river widths into equation (4.7). PS YG and PS YP, hence, exhibit the same river widths but differ in the way how river depth was obtained.

4.2.3.2.2 Data post-processing

Spatial differences between input rasters and the 1D channel network required additional processing steps. Besides, DEM irregularities along the river path and dissimilarity between the parameterization strategies induced also the need for data processing.

4.2.3.2.2.1 Upstream drainage area filtering in PS GG and PS PP

The upstream drainage area raster was used, as described above, to both link its values for downscaling purposes (PS GG) and directly to river width and depth (PS PP). Both approaches extract the value of the raster cell at the location of each sample point along the 1D channel network. However, in some cases, the sample points on the 1D network do not coincide with the river stream represented by the accumulated upstream drainage area raster (Figure 4.4). Due to the sinuosity of the 1D network, the sample point may lie on the raster cell adjacent to the main accumulation path. For example, an upstream drainage area of 5.7 x 10^6 m^2 (highlighted in yellow) is extracted which results for instance by applying equation (4.5) from PS PP in a river width of two meters. However, a river width of two meters for the Amazon River near the river mouth is highly unlikely and would further create a bottle-neck effect. To avoid such distortions in river width and depth along the 1D channel network, a filter at the location of each sample point was applied, extracting the highest raster value within a 3x3 window (Figure 4.4). In the example of Figure 4.4, by applying the filter an upstream drainage area of 5.9 x 10^{12} m^2 (highlighted in red) is extracted which results in a river width of 3,070 meters instead.

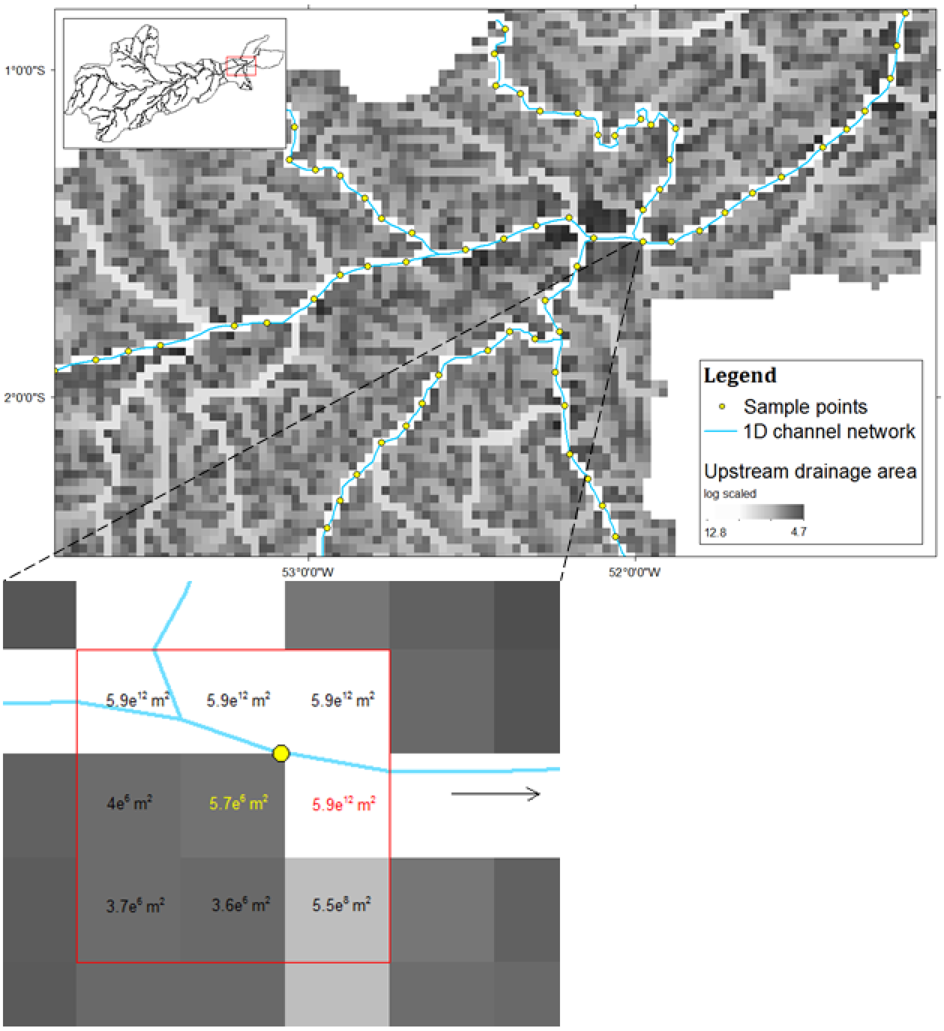

Figure 4.4: Applied filter extracts at each sample point the highest upstream area within a 3x3 window.

4.2.3.2.2.2 DEM smoothing along the river path

At each sample point location, the surface elevation from the DEM is extracted and stored as attribute in the sample point file. The required river bed elevations were then derived by subtracting the river depth from the surface elevation at each sample point. Therefore, water surface elevations of the river itself were needed which we assume to be identical with the elevation of the SRTM DEM as the radar signal is not able to penetrate water bodies. Even though vegetation canopy was removed, systematic errors related to vegetation on the river banks, surface water effects, and also random error related to noise in the DEM data introduce elevation irregularities along the river, thus possibly deteriorating the quality of our bathymetry calculations (Paiva et al., 2011b; Yamazaki et al., 2017). To ensure flow connectivity on the DEM along the 1D river network, surface elevations in the DEM were smoothed using the algorithm proposed by Yamazaki et al. (2012a). This algorithm either 'digs' or 'fills' the elevation values along a one-dimensional streamline on a drainage network. More specifically, it aims to remove the pits in a DEM, that is a pixel which is surrounded by pixels with higher elevations, with the least required modification steps. Consequently, the adjusted DEM is kept as close to the original values as possible (Yamazaki et al., 2012a). In this study, only raster cells covered by the densest 1D channel network (N001) were smoothed to maintain most of the original surface elevation values in the DEM (shown as gray cells in the small raster in Figure 4.5). Figure 4.5 illustrates the surface elevations extracted from the DEM at the sample point locations along a certain flow path from the original (canopy removed) DEM and from the smoothed DEM. Finally, the smoothed river surface elevations were then used to derive the river bed elevations by subtracting smoothed surface elevation and river depth.

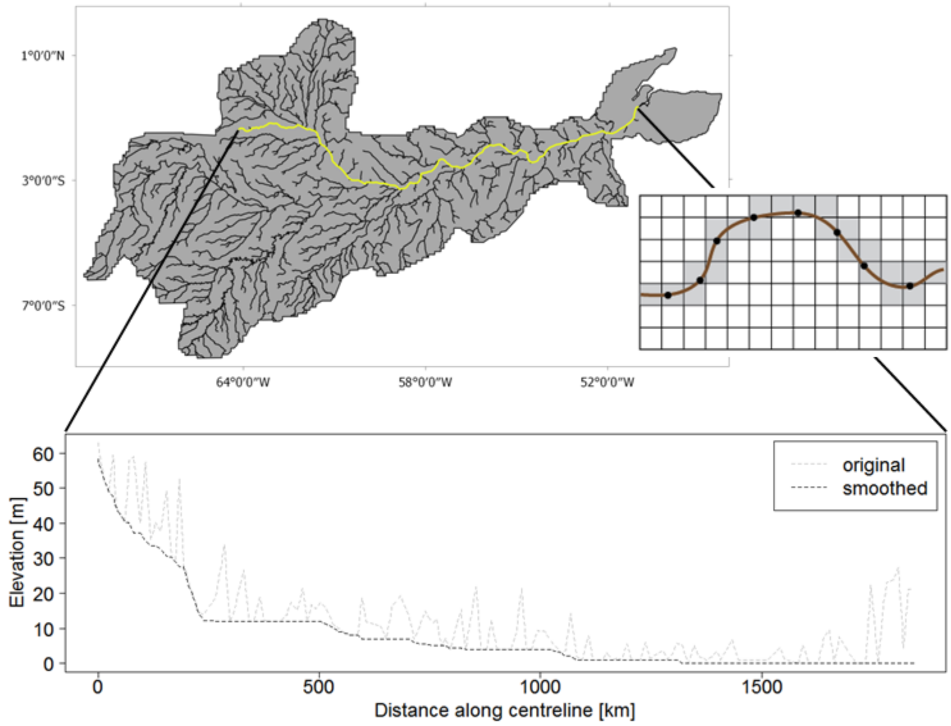

Figure 4.5: Original and smoothed surface elevations extracted at each sample point location along a certain flow path (yellow line). Small raster on the right-hand side shows the concept of surface elevation smoothing: only DEM cells representing the river channel (gray cells) are smoothed and then extracted at the location of each sample point.

4.2.3.2.2.3 Accounting for lakes in PS YG and PS YP

The GWD-LR database from Yamazaki et al. (2014a) calculates the river width based on SRTM Water Body Data. Yet, this water body mask not only contains rivers but also lakes. PS YG and PS YP result therefore in enormous river widths (up to ∼22 km) as well as river depths (up to 82 m). These lakes create great dead storage volumes which have to be filled first with water in order to enable water to flow further downstream along the channel (see fictive example in Figure 4.6). PS GG and PS PP, however, do not take these lakes into account. In order to ensure consistency throughout all parameterization strategies, sample points representing large lakes in PS YG and PS YP were manually manipulated. Only sample points which exhibit river widths larger than 8,000 m were inspected with OpenStreetMap and its bed elevations altered. River width, however, remained unaltered to contain the purpose of using widths determined by the GWD-LR. The threshold of 8,000 m was arbitrarily chosen and had the purpose to select a reasonable amount of sample points which could be manually manipulated. OpenStreetMap showed that some sample points exceeding river widths of 8,000 m agreed well with actual river widths and that not all sample points above the threshold represent lakes. Therefore, sample points needed to be inspected and altered individually which in turn precludes the usage of a more automatic procedure to cope with dead storages due to lakes. The new bed elevation of the sample points describing lakes was obtained by linear averaging of the bed elevations of the adjacent up- and downstream sample points (Figure 4.6). If there was no further upstream sample point, for instance at the end of a river branch, bed elevation was then lifted to the bed elevation level of the downstream sample point. A list of all sample points whose bed elevations were altered (averaged) is given in Appendix A.

Figure 4.6: Fictive illustration of dead storage along the channel path where downstream bed elevation is higher than the upstream. Dead storages due to lakes were adjusted by averaging the bed elevations of the adjacent up- and downstream sample points (red dot).

4.2.3.2.2.4 Interpolation of river bed elevations and widths to DFM

Assigning river bed elevations and river widths to the 1D computational nodes in the hydrodynamic model DFM takes place throughout a model internal interpolation of the sample points. The interpolation methods between bed elevations and river widths differ though. River bed elevations from the sample points are assigned to the 1D computational nodes via (2D-)spatial interpolation such as triangulation or cell averaging. The interpolation of the river width samples, in turn, takes place via linear interpolation in between the sample points along the 1D river branches.

The spatial interpolation method for the bed elevations creates a problem for one-dimensional applications because the bathymetric information on spatially different river branches will interact the interpolation. Desirably, bed elevations from the sample points are linearly interpolated along each 1D river branch without any interference from nearby sample points located on other river branches. This is, however, not the case because of the spatial interpolation and further adaptation of the bed elevation sample points is required. To prevent the interpolated bed elevation to be biased from bed elevations belonging to adjacent river branches, additional sample points were created as a buffer around each river branch (Figure 4.7). To that end, sample points were firstly rasterized to a grid. Between the sample points along the river, the bed elevations were then linearly interpolated. Subsequently, a buffer around each river branch was created where the interpolated values from the adjacent raster cells were assigned to. In order to cope with overlapping buffers at river confluences, river branches had to be buffered stepwise according to its Strahler order, starting from low to high Strahler order. In this manner, the buffer of a river branch having a high Strahler order was favored over those with a low Strahler order. Finally, the raster cells containing bed elevation values (i.e. buffer and river) were converted back into a DFM compatible format (Figure 4.7).

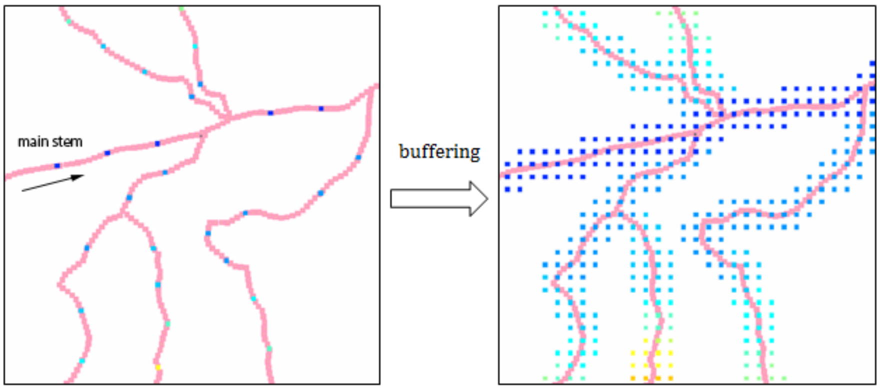

Figure 4.7: Left-hand side: original distribution of the sample points containing bed elevations. At the confluences of river branches or where river branches are spatially close to each other, the interpolation of bed elevations on each river branch will be negatively impacted due to the other one. Right-hand side: additional sample points arranged as a buffer.

4.2.4 Defining roughness coefficient and downstream boundary condition

The roughness coefficient Manning's n for the channel was uniformly set to 0.03 s $m^{-1/3}$. DFM does not allow for spatially varying floodplain friction coefficients and hence also a uniform value for the entire 2D domain was used and set to 0.08 s $m^{-1/3}$. This is in accordance with values used in other studies in the Amazon Basin (LeFavour and Alsdorf, 2005; Trigg et al., 2009; Rudorff et al., 2014; Hoch et al., 2017a). Besides the friction coefficients for channel and floodplain, open boundary conditions defined downstreams where the Amazon River drains into the sea are required in order to enable water to flow out of the system. Further, tidal and surge motions towards the land can be described by the downstream boundary conditions. Even though the sea-tide influence on the hydrodynamics of the Lower Amazon is known to be significant (Kosuth et al., 2003, 2009), we excluded the tidal forcing in this study and defined a constant water level of 0 m as downstream boundary condition.

4.3 Analysis

4.3.1 Sensitivity analysis

4.3.1.1 Boundary conditions

Water can be supplied to DFM by discharge or rainfall boundary conditions. Discharge boundary conditions operate outside the model domain and supply the model with water input from discharge timeseries by means of spatially defined polylines. To deliver water to all river branches, especially to those which lie completely within the model domain, might not be suitable by means of discharge boundary conditions. Thus, a synthetic rainfall event was set up to supply DFM with water over the entire 1D/2D model domain. The simulation time of three years was randomly chosen but aimed at allowing a sufficient timeframe for the hydrologic response in such a large area. A spatially and temporally uniform rainfall event (10 mm day^{-1}) over the entire 1D/2D model domain was inserted after the first half year for a period of six months (Figure 4.8). The rainfall amount of 10 mm day^{-1} for a period of six months was chosen after trial and error to avoid supplying too much water in which river channel and floodplain is completely flooded.

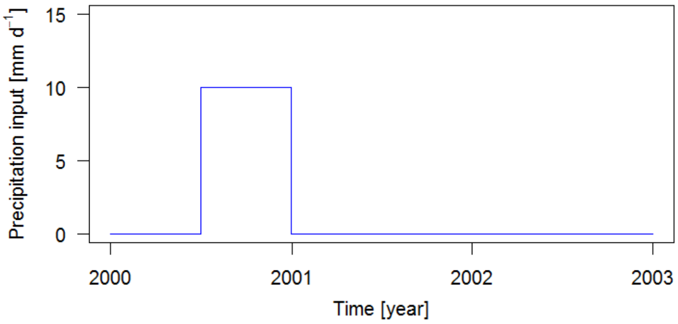

Figure 4.8: Synthetic rainfall of 10 mm day^{-1} for a period of six months was inserted over the entire 1D/2D model domain in DFM.

4.3.1.2 Initial conditions

To represent a perennial river as realistically as possible, the simulation preferably starts with initial water in the river channels. Starting with dry initial conditions for the 1D channels might also cause water to be stored in the channels due to dead storages as a result of varying river bed elevations. This could bias the response of the different 1D networks as the densest network (N001) will have more channels and hence possibly greater dead storage volumes compared with the smaller network extents. To reduce the possibly biased response caused by these dead channel storages, initial model runs for all schematizations were performed to obtain model states at the last time step to be used as restart files. The last time step of the initial model runs shows the residual water which could not drain because of local elevation depressions in both the 1D and 2D domain. These restart files were then inserted as initial water condition for the new model runs. The drawback of using the aforementioned restart files is that not only the 1D channels but also the 2D floodplain receives initial water. As a consequence of the various 1D network extents, the residual water depths on the floodplain vary among the schematizations. Figure 4.9 illustrates the resulting initial water conditions on the 2D domain for the networks N001 and N10. These differences in initial water depths on the floodplain might bias the hydrologic response among the schematizations because friction on the floodplain is lessened with an increase in water depth and might lead to less conclusive results regarding the model sensitivity to the 1D network densities. The sensitivity analysis was thus performed for both, with and without the usage of the restart files.

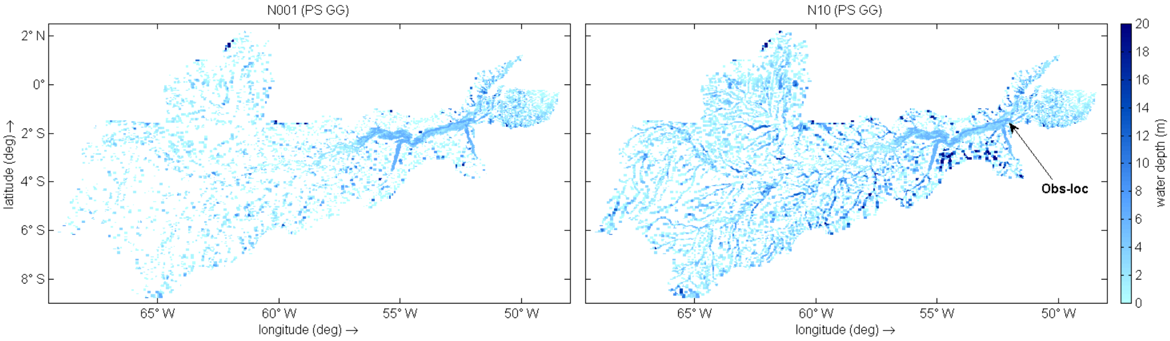

Figure 4.9: Initial water depth on the 2D floodplain at time step t_0 for the densest network N001 (left-hand site) and sparsest network N10 (right-hand site).

4.3.1.3 Model variables

With respect to the model outputs, only flood wave propagation and attenuation, and water level were examined in the delta region of the Amazon River (obs-loc in Figure 4.9). Flood extent was excluded in this case because water was supplied and discharged over the entire 1D/2D model domain. The main attention was on how the hydrologic response observed in the downstream part of the study area is affected by the different schematizations.

4.3.2 Accuracy analysis

4.3.2.1 Boundary conditions

The coupling between DFM and PCR was achieved by means of the basic model interface (BMI) (Hoch et al., 2017a). The BMI facilitates the information exchange between models at any given time step and for any model internal state variable. By coupling models to a BMI, internal state variables can be retrieved, manipulated, and re-inserted into the original model or used to overwrite variables in another model. Because of the possibility to update models connected to a BMI at a user-specified timestep, the manipulation of the state variables is feasible during the execution of the models in use (Hoch et al., 2017a). PCR and DFM were coupled where the cells of both models spatially overlay. With regard to the model domain in DFM, PCR was coupled to the 1D network. This means that all computational nodes of the 1D network in DFM which lay within a PCR cell were connected and received water input from this specific PCR cell. To this end, both models run simultaneously whereby within the coupled area water input from PCR to DFM was updated on a daily basis. PCR run spatially for the entire Amazon Basin (Figure 3.1) calculating surface runoff on a cell-by-cell basis and subsequently routing water along an LDD my means of the kinematic wave approximation towards the model domain of DFM. If the routed water in PCR reached the overlapping model domain where the coupled model cells were present, no further routing along the LDD in PCR was performed. Instead, the available water volume (i.e. river discharge inflow and local surface runoff) in the PCR cells were divided over and added to all computational nodes in DFM within the respective PCR cells. Yet, the coupling only took place one-directionally where information from PCR was transferred to DFM without the possibility to reversely exchange information (Hoch et al., 2017a). Consequently, water added to DFM can only be discharged, excluding further infiltration or evaporation in the channel or on the 2D floodplain in case of flooding. This may cause an overestimation of modelled discharge, water depth, and inundation extent. For further information about the BMI and the coupling framework, this study refers to Hoch et al. (2017a).

The described coupled model run was performed for the time period 2004 to 2009 with the first year being used for spin-up of the coupled settings. This time period includes the severe flood event which occurred in 2009 (Paiva et al., 2013a). The central and northern region of the Amazon Basin experienced extensive flooding which created many casualties and left more than 376,000 people homeless (Chen et al., 2010).

4.3.2.2 Model variables

Discharge, inundation extent and water level were modelled in DFM for the time period 2005 to 2009 and validated against observations. Simulated discharge was compared with observed discharge at the station Obidos (Figure 3.1). In addition, to validate high and low water flows separately, the simulated discharge time series were separated by the observed mean discharge into high and low water. The root mean square error (RMSE) and the Kling-Gupta efficiency (KGE) (Gupta et al., 2009) provided measures for the overall performance of the hydrographs and the model's skill, respectively. The RMSE is defined as:

$$RMSE = \sqrt{\frac{1}{T}\sum_{t=1}^{T}(S_t - O_t)^2}, \tag{4.8}$$

where S_t is the simulated discharge at time step t, O_t is the observed discharge at time step t, and T the total number of time steps. KGE, in turn, is given by:

$$KGE = 1 - ED, \tag{4.9}$$

with
$ED = \sqrt{(r-1)^2 + (\alpha-1)^2 + (\beta-1)^2}$
r = Pearson product-moment correlation coefficient
$\alpha = \sigma_s/\sigma_o$
$\beta = \mu_s/\mu_o$

where σ_s and σ_o denote the standard deviation of the simulation and observation, respectively. μ_s and μ_o are the simulated and observed mean.

The RMSE states the mean deviation of the simulated to the observed values and has the same units as the quantity being evaluated. Hence, the lower the RMSE value, the smaller the differences between simulated and observed values. KGE, in turn, considers three components to measure model performance which are variability, bias and correlation. The components variability and bias compare simulated and observed standard deviations and means, respectively. Further differences between simulated and observed, such as timing of the peaks, and shapes of the rising and falling limb of the hydrographs, are analyzed by the correlation coefficient (Gupta et al., 2009). These three components are then combined and yield the KGE in which a value of one is ideal. Modelled water level was also compared at the station Obidos with observed water level. Both, observed discharge and water level data at Obidos were derived from the Observation Service SO HYBAM. Simulated water levels in DFM ranged between 21 m and 27 m whereas the measured ones at Obidos ranged between 0 m and 9 m. This discrepancy could be caused by elevation errors in DFM introduced by the SRTM DEM as we only smoothed DEM values along the 1D channels. In order to still allow for comparability between simulation and observation, water levels were normalized by subtracting the respective means from both data sets. By doing so, timing and amplitude of the water levels remain comparable.

Regarding the inundation extent, satellite imagery was used to provide validation data. To perform a comprehensive flood extent validation, the entire study domain was included. The validation of inundation extent was performed for the flood event in 2009. According to Chen et al. (2010), the flood began in early 2009 and reached the maximum in March 2009 in the northern Amazon. The flood continued into July in the central Amazon where the study domain is situated. The Global Surface Water dataset (Pekel et al., 2016) provides, among many other products, monthly water body layers derived from an extensive collection of Landsat 5, 7, and 8 images. These water body layers are binary maps in which each pixel is either classified as water or no water. The frequent occurrence of cloud cover in humid tropical regions such as the Amazon is known to severely hamper the usage of optical remote sensing (Asner, 2001; Brivio et al., 2002). As a result, the monthly water body layers from the Global Surface Water dataset may contain substantial amount of unclassified pixels due to cloud cover. In order to deal with that, water body layers from multiple months were merged together illustrating the maximum inundation extent which occurred within the months. This was achieved by producing a new water body layer in which a pixel was classified as water if the pixel in one of the months was once classified as water. The months May to July 2009 were chosen for the benchmarking flood extent map. In DFM, simulated inundation depicting the water situation in July 2009 was extracted and used for validation. Inundation extent did not change spatially in DFM over the period May to July 2009 and hence the single date (July 2009) was considered to be sufficient for the validation procedure. Subsequently, the agreements between simulated and observed inundation extent were assessed using measures of hit rate (Hr), false alarm rate (Far) and critical success rate (Csr) according to the following relations (Hoch et al., 2017b):

$$Hr = \left(\frac{N_S \cap N_O}{N_O}\right) 100, \tag{4.10}$$

$$Far = \left(\frac{N_S \setminus N_O}{N_S \cap N_O + N_S \setminus N_O}\right) 100, \tag{4.11}$$

$$Csr = \left(\frac{N_S \cap N_O}{N_S \cup N_O}\right) 100, \tag{4.12}$$

where N_S and N_O indicate the number of simulated and observed inundated cells, respectively. Hit rate indicates the agreement between simulated and observed flooded cells. The number of cells which were only flooded in DFM but not in the benchmark map are provided by the false alarm rate. The latter of the three, critical success rate, gives the overall performance between cell agreements and cell mismatches.

Chapter 5

Results

5.1 River network parameterizations

PS PP relates river width and depth to upstream drainage area which leads to a continuous increase of river width and depth with flow distance. Compared to this, river width and depth were calculated from discharge in PS GG, producing more variation along the channel network than PS PP. This is mainly because discharge was derived from average long-term annual runoff simulated by PCR and upstream drainage area. Runoff is an integrated component of the water balance equation and depends on precipitation, evapotranspiration, soil water storage, and groundwater storage. Therefore, runoff as well as the obtained bathymetry may transit less smoothly from upstream to downstream. Empirical equations, however, are not able to capture the local variability of river channels and may thus be not realistic for many river reaches (Yamazaki et al., 2014a). In PS YG and PS YP, satellite imagery is used to obtain river widths which in turn results in a better representation of the river channels than PS GG and PS PP (Figure 5.1). Especially the river widths of the Negro River are not captured by the last two. Figure 5.1 illustrates also that the water body mask, on which the river widths in PS YG and PS YP are based, includes lakes as well as island gaps where the latter will cause oversized channel widths (see downwards part from the confluence at Manaus).

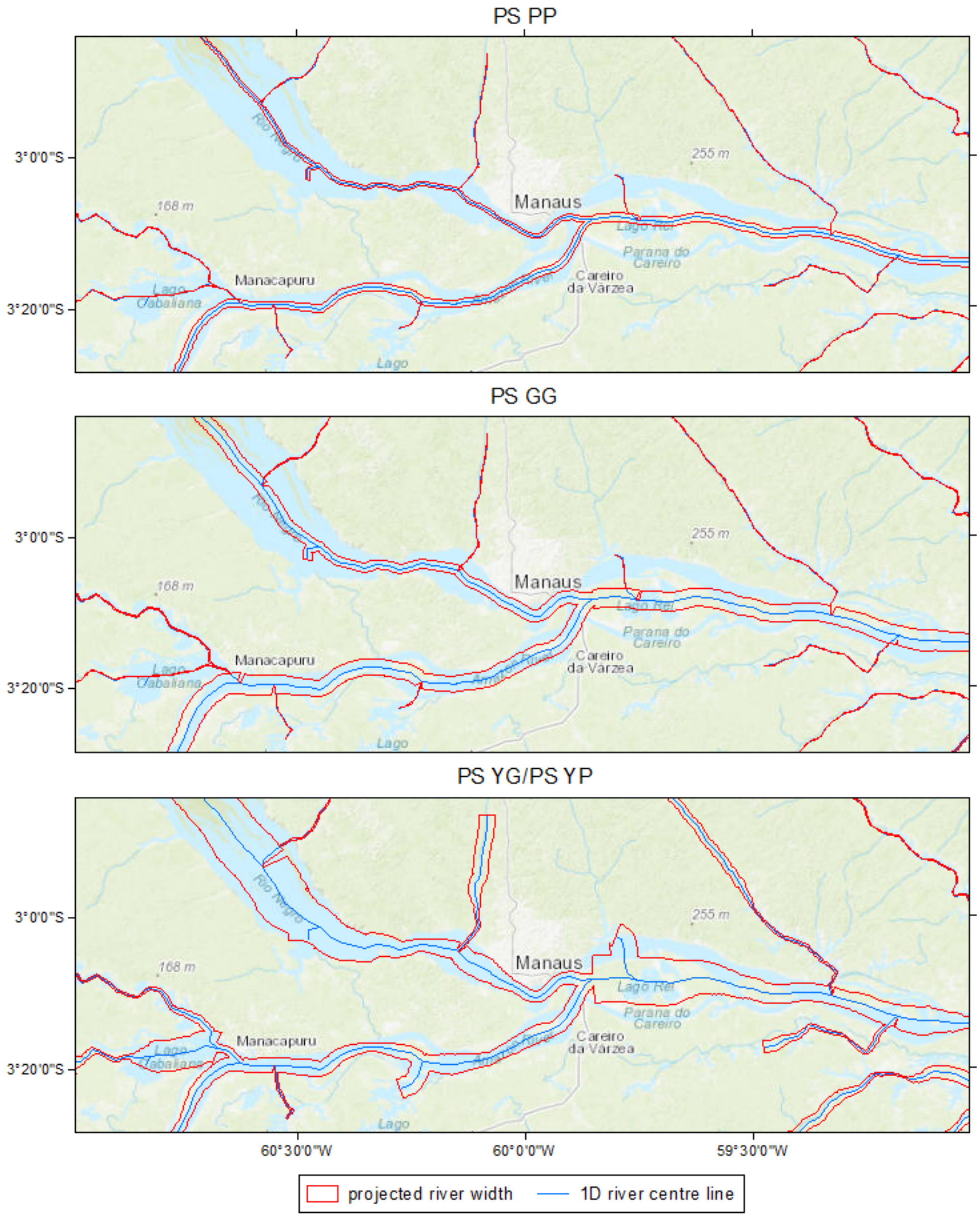

Figure 5.1: Projected river widths derived from empirical relationships (PS PP, PS GG) and satellite imagery (PS YG/PS YP). The Figure shows the area where the Negro River meets the Solimoes River at Manaus.

Table 5.1 provides descriptive statistics, that is minimum, maximum, mean, and standard deviation, for river width and depth resulting from the different parameterization strategies on the densest river network (N001). PS PP shows the smallest widths with a mean of 288 m as well as the lowest variation (SD 540 m). In turn, river widths derived from remote sensing show the largest widths (22,148 m) and greatest variation (SD 2,107 m). The river widths obtained by PS GG are situated somewhere in between these two. Regarding the river depths, greater depths are generated by PS PP than by PS GG. PS YG and PS YP have both the same river width but by linking river widths to depths via equation (4.7), a deeper river channel will be created than with equation (4.4) (mean depths of 16 m and 5 m in PS YP and PS YG, respectively).

Table 5.1: Descriptive statistics (in meters) for river width and depth derived from the four parameterization strategies on the densest river network (N001).

	PS GG		PS PP		PS YG		PS YP	
	Width	Depth	Width	Depth	Width	Depth	Width	Depth
Min	33	2	24	5	31	2	31	5
Max	8933	33	3068	28	22148	61	22148	51
Mean	747	4	288	9	1241	5	1241	16
SD	1350	5	540	5	2107	7	2107	8

As a result of the differences in river width and depth, all parameterization strategies exhibit also diverse storage volumes of their channel networks (Table 5.2). For almost all river network densities, the channel storage volumes increase in the following order; PS PP, PS GG, PS YG, and PS YP. This order agrees with the aforementioned width and depth characteristics of the different approaches. Interestingly, the storage volume for the densest network (N001) in PS PP is larger than in PS GG while for the other three network densities (N01, N1, N10) PS GG leads to larger channel storage volumes. Table 5.2 reveals that the width-depth equations (4.4) and (4.7) result in widely different storage capacities (see PS YG and PS YP in Table 5.2).

Table 5.2: Channel storage capacities (in km^3) of each river network parameterization.

	PS GG	PS PP	PS YG	PS YP
N001	486	493	983	1952
N01	439	376	767	1353
N1	412	292	588	948
N10	341	200	349	567

5.2 Sensitivity analysis

5.2.1 Model runs with initial water depths in the 1D/2D domain

5.2.1.1 Discharge at observation location

The resultant river discharges for all imposed schematizations at the observation location (obs-loc in Figure 4.9) are presented in Figure 5.2. Figure 5.2 illustrates for each parameterization strategy the outcomes from the four 1D network densities. For an optimized visualization of the graphs, only the period including the rising and falling limb of the flood hydrograph is plotted. The shapes of the hydrographs in terms of flood wave propagation and magnitude resulting from the different schematizations look near-identical. For all parameterization strategies, the densest network (N001) responds most rapidly to the rainfall event. The differences to the other network extents, however, are very small. The densest network (N001) leads only in PS GG and PS PP to a higher peak discharge. In PS YG and PS YP, peak discharge in N001 is attenuated. In return, a higher amount of water is drained during the falling part of the hydrograph when more channels exist (N001). This is the case for all parameterization strategies. The densest network (N001) leads in all parameterization strategies to the highest cumulative discharges. Even though peak discharge in PS YG and PS YP in N001 is attenuated, yet these two yield the highest cumulative discharges of 1.76 x 10^{12} m^3 and 1.78 x 10^{12} m^3, respectively.

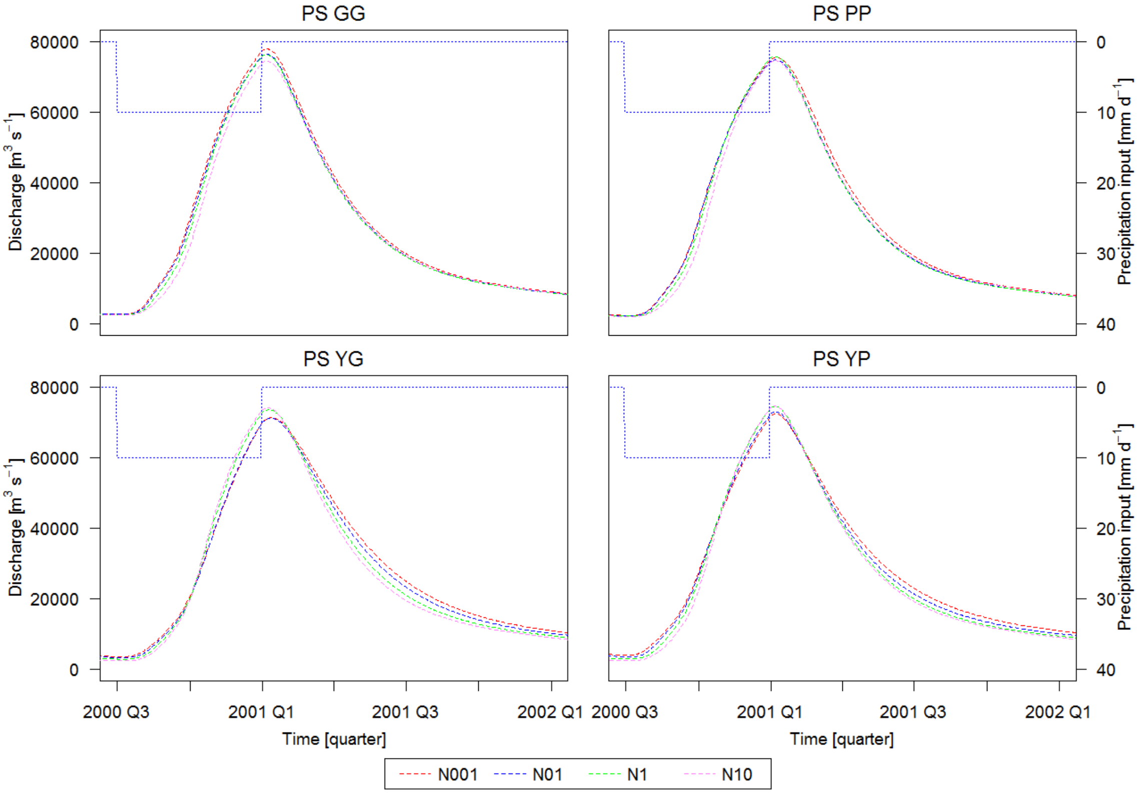

Figure 5.2: River discharge at the observation location (obs-loc) illustrated for each parameterization strategy and the respective 1D networks. Model runs were initialized with water depth from restart files to provide the 1D channels with initial water.

The same results as in Figure 5.2 are shown in Figure 5.3 but plotted in respect of the 1D network densities. It becomes apparent that the variation of the flood hydrographs between the parameterization strategies increases with an increase in channel density. For the same network density, PS GG leads to the highest peak discharge followed by PS PP, PS YP, and then PS YG. This order is consistent for the networks N001, N01, and N1. Regarding the falling limb of the hydrograph, the above mentioned order is reversed whereby PS YG drains the greatest amount of water. Furthermore, the flood hydrographs are hardly distinguishable from each other in the sparsest network (N10).

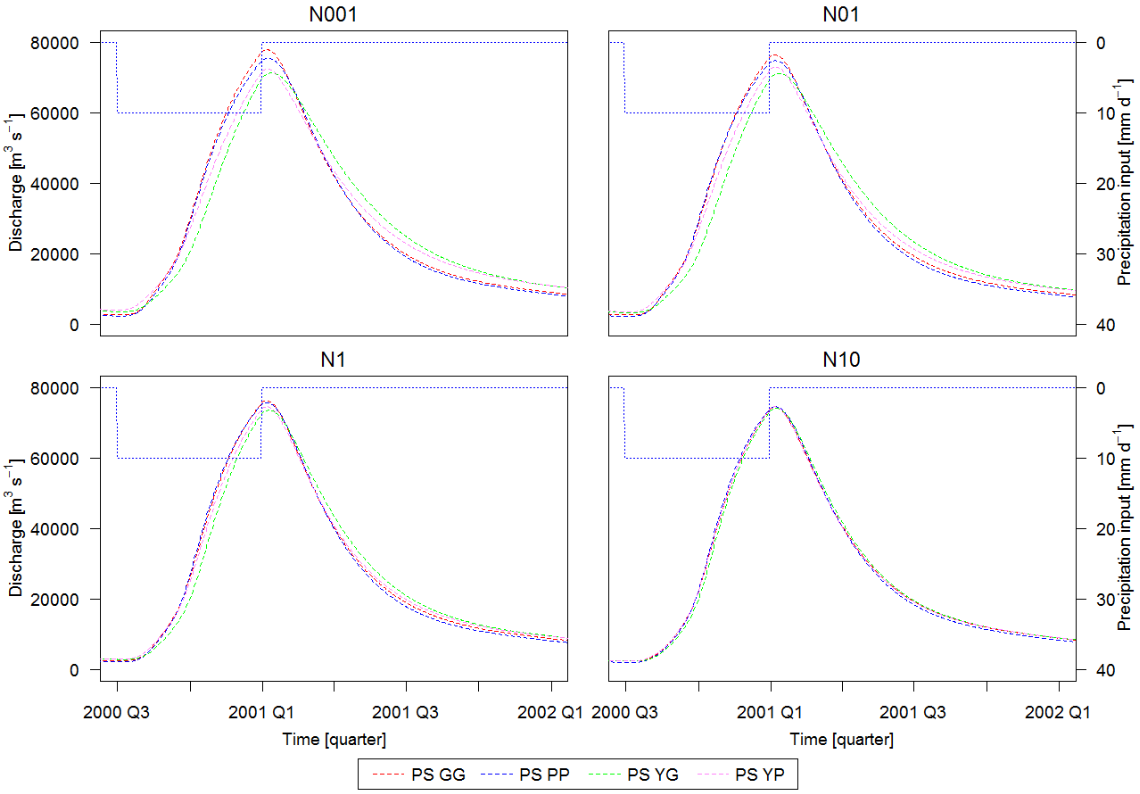

Figure 5.3: River discharge at the observation location (obs-loc) illustrated for each 1D network extent and the respective parameterization strategies. Model runs were initialized with water depth from restart files to provide the 1D channels with initial water.

5.2.1.2 Water level at observation location

The findings at the observation location in the downstream part of the study area reveal that the water level amplitude decreases with an increase in channel density (Figure 5.4). In PS YG and PS YP this reduction in the water level amplitude is more pronounced than in PS GG and PS PP. The same pattern occurs when the resultant water levels among the parameterization strategies are compared. There are almost no differences between the parameterization strategies in the sparsest network (N10) but with a higher channel density, the distinctions become clearer. The water level amplitude in PS GG and PS PP for the densest network (N001) is very similar and larger than the amplitudes of PS YG and PS YP.

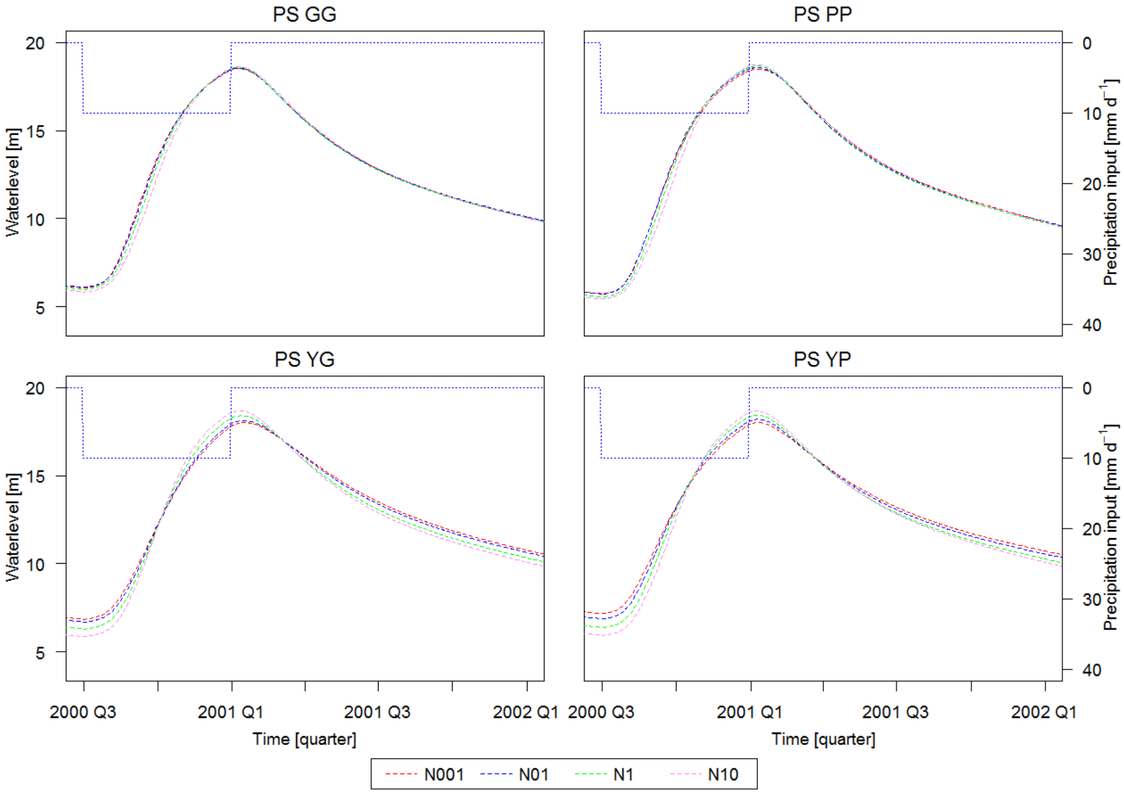

Figure 5.4: Water level at the observation location (obs-loc) illustrated for each parameterization strategy and the respective 1D networks. Model runs were initialized with water depth from restart files to provide the 1D channels with initial water.

5.2.2 Model runs without initial water depths in the 1D/2D domain

5.2.2.1 Discharge at observation location

In the second case, the model schematizations were run without initial water depth (i.e. without restart files) meaning that the 2D floodplain was completely dry at the beginning of the simulation. The same does not necessarily apply to the 1D channels since DFM fills automatically all channels which lie below the water level of 0 m specified in the downstream boundary condition (Chapter 4.2.4). The results from the model runs without initial water depths are presented in Figure 5.5. The densest network (N001) generates in all parameterization strategies the greatest amount of discharge. In PS GG and PS PP, the water surplus indicated as mean relative difference between N001 and N10 accounts to 94% and 81% respectively. The mean relative differences in the two other parameterization strategies, PS YG and PS YP, between N001 and N10 are in the order of 72% and 80%, respectively. The densest network (N001) responds most rapidly to the rainfall event in all schematizations. This early response to the rainfall event is reflected in a very steep rise in PS GG and PS PP, whereas in PS YG and PS YP the rising limb of the hydrograph is more curved and the response thus more decelerated. The flood peak in all parameterization strategies arrives approximately one month earlier in the densest network when compared with the sparsest network.

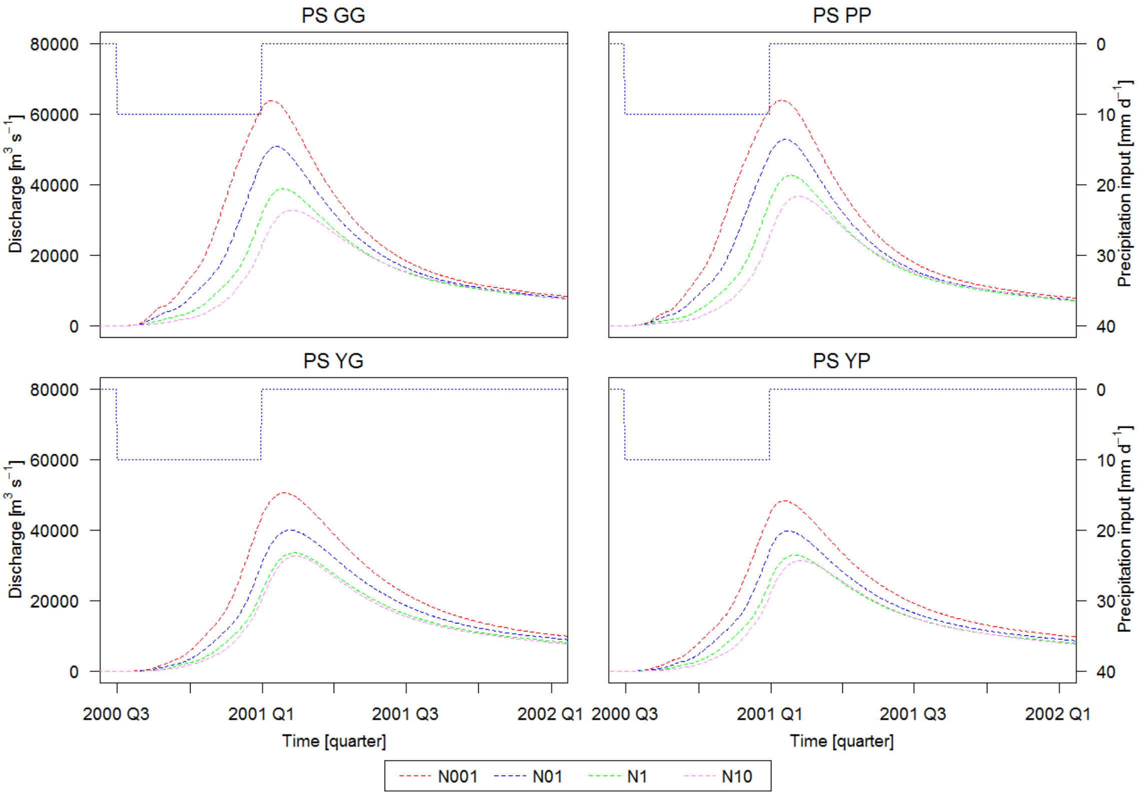

Figure 5.5: River discharge at the observation location (obs-loc) illustrated for each parameterization strategy and the respective 1D networks. In this case, model runs started with dry conditions (i.e. without restart files).

Figure 5.6 shows clearly the difference in response time between PS GG/PS PP and PS YG/PS YP for especially the densest network (N001). Similar to the pattern in Figure 5.3, the differences among the parameterization strategies becomes more pronounced with an increase in channel density. Besides the response timing, also the peak discharges differ. Compared with PS YG, the peak discharge in PS GG is increased by around 30% in the densest network (N001). Regarding the cumulative discharges between the parameterization strategies, PS GG in N001 exhibits the largest amounts of 1.33 x 10^{12} m^3. In the other three 1D networks, however, PS PP drains the largest amount of discharge and exhibits also the highest peak discharge.

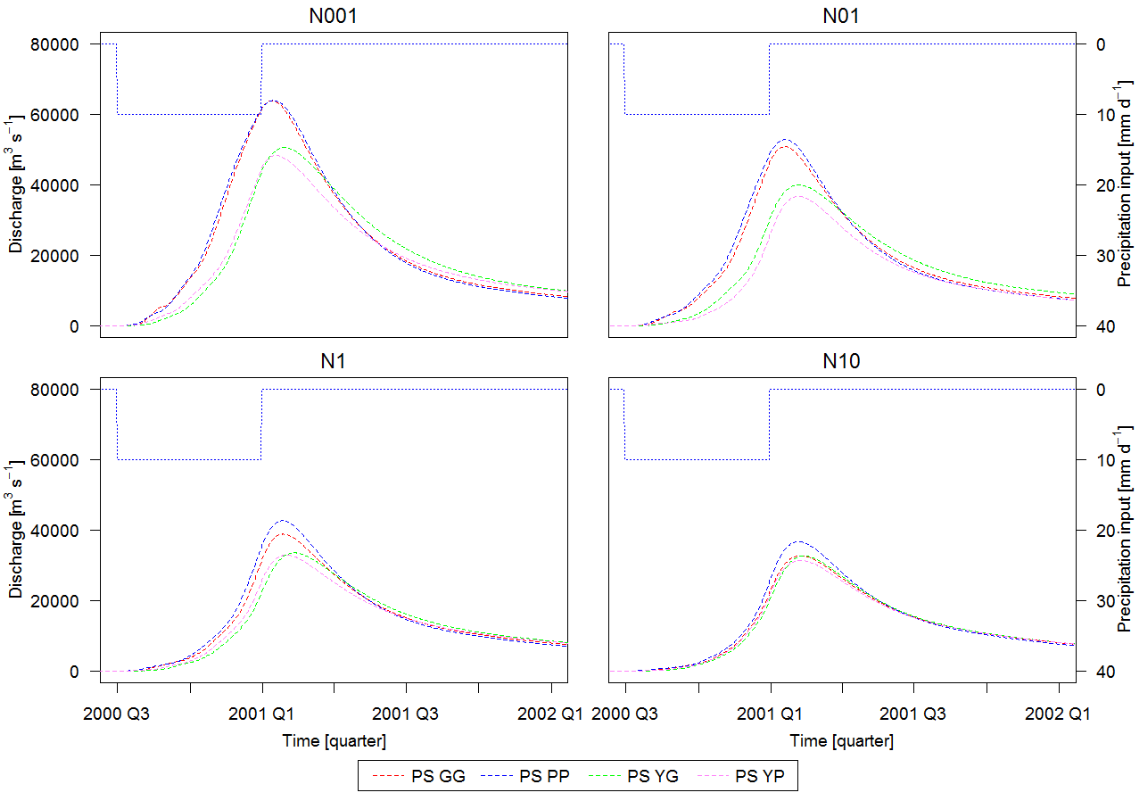

Figure 5.6: River discharge at the observation location (obs-loc) illustrated for 1D network extent and the respective parameterization strategies. In this case, model runs started with dry conditions (i.e. without restart files).

5.2.2.2 Water level at observation location

Likewise the previously observed pattern, Figure 5.7 illustrates the water levels from implemented schematizations in which the water level variation is more pronounced for the densest network (N001) compared with the other networks. Also for each parameterization strategy, the densest network (N001) responds most rapidly and generates the highest water levels. With regard to the parameterization strategies, PS PP leads in all network densities to the highest water levels and responds most rapidly to the rainfall event.

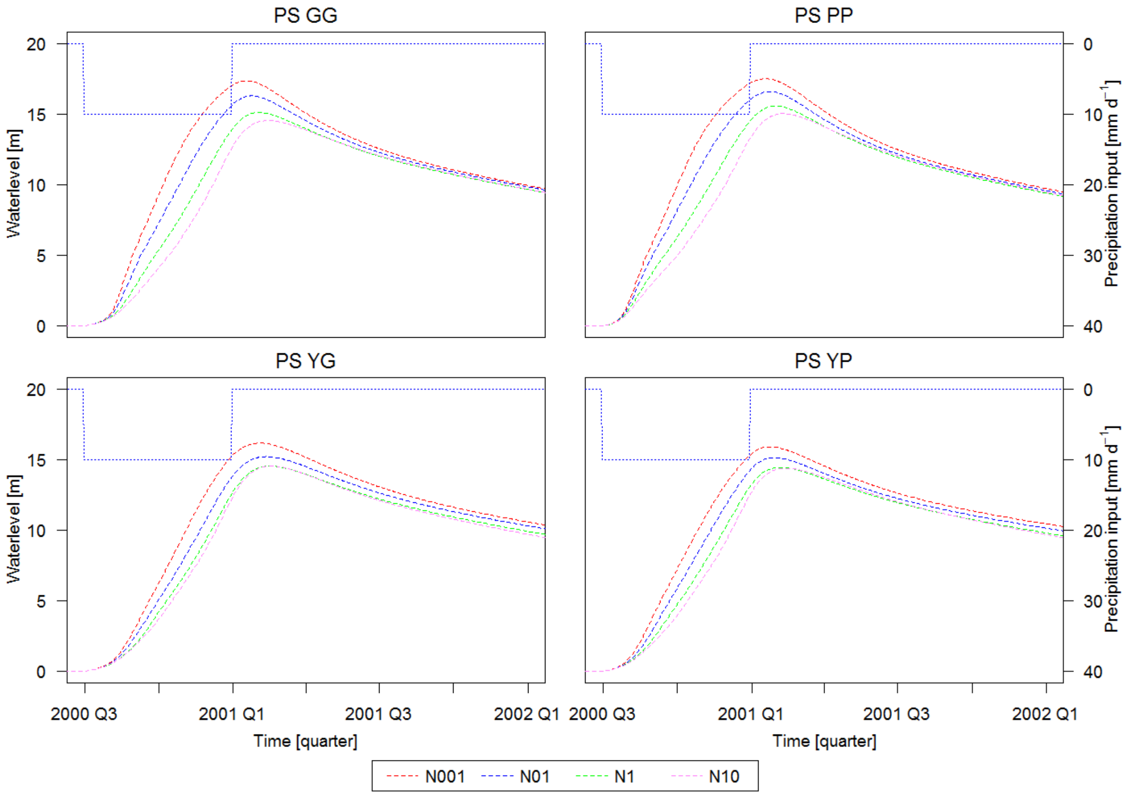

Figure 5.7: Water level at the observation location (obs-loc) illustrated for each parameterization strategy and the respective 1D networks. In this case, model runs started with dry conditions (i.e. without restart files).

5.3 Accuracy analysis

5.3.1 Discharge at Obidos

Simulated and observed discharge at Obidos for the time period 2005 to 2009 are plotted in Figure 5.8. From a visual point of view, all schematizations perform fairly well when compared with observed discharge. This is especially evident in the first half of the simulation period for the high water flows of the Amazon River. In the second half of the simulation, that is from 2008 onwards, the schematizations overpredict the peak discharge. In addition, all schematizations overestimate constantly the low water flows of the Amazon River during the dry seasons. The mean relative difference between two hydrographs indicates the mean increase (or decrease) of one hydrograph over the other one. The hydrograph from the densest network for all parameterization strategies increases by around 8% (mean relative difference) when compared with the hydrograph from the sparsest network (N10). A similar pattern between the networks is visible which applies to all parameterization strategies. During the rising limb of the hydrograph, there are hardly any differences recognizable between the network extents. For the peak and the falling limb of the hydrograph, however, the densest network (N001) yields more discharge than the sparsest one. Distinctions between the parameterization strategies are discernible for instance for the high water flows in 2005 and 2006 in which PS GG and PS YP seem likely to be closer to the observations than PS PP and PS YG. In addition to Figure 5.8, the same results are plotted with respect to the network densities in Figure B.1 in Appendix B.1.

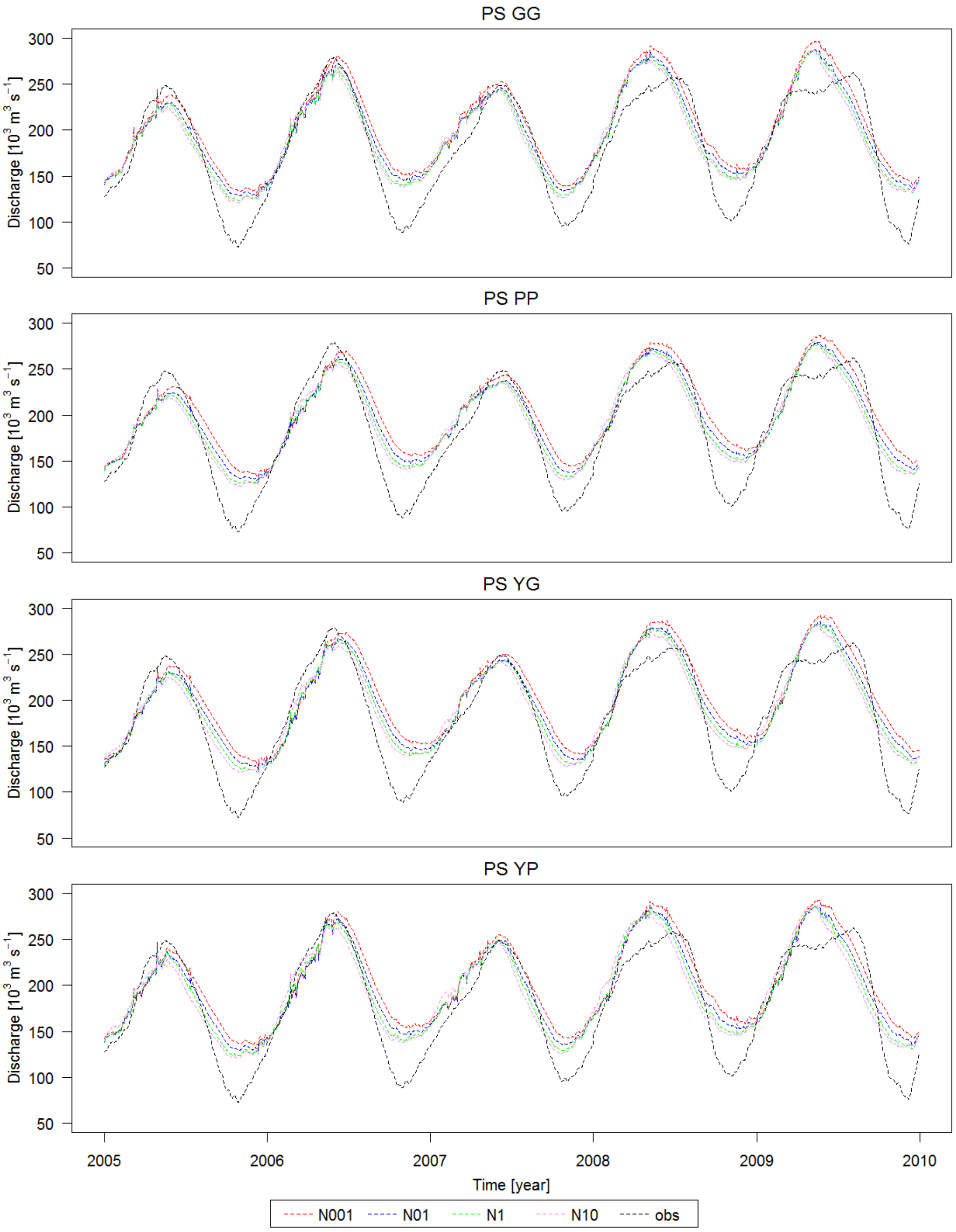

Figure 5.8: Observed and simulated discharge at Obidos.

Table 5.3 provides the resultant RMSE and KGE for all schematizations. The RMSE is lowest for all parameterization strategies in the sparsest network (N10) and increases with an increase in channel density. The differences between the parameterization strategies are not as pronounced than between the network extents. Contrary to this, KGE values show a higher variation between the parameterization strategies than between the network densities. Overall, KGE values range between 0.69 and 0.77 indicating that all schematizations perform fairly well. The best model performance with respect to the KGE is achieved by PS YG and PS YP on network N1 (KGE 0.77) whereas parameterization strategy PS PP on network N001 performs worst (KGE 0.69). Parameterization strategy PS YG on the sparsest network, in turn, yields the lowest RMSE of 24,707 m^3.

Table 5.3: Root mean square error (RMSE) and Kling-Gupta efficiency (KGE) obtained to evaluate discharge.

	RMSE				KGE			
	PS GG	PS PP	PS YG	PS YP	PS GG	PS PP	PS YG	PS YP
N001	30886	33825	34778	31903	0.75	0.69	0.73	0.73
N01	27420	28738	29632	27508	0.75	0.70	0.74	0.74
N1	25863	26081	26293	25433	0.76	0.72	0.77	0.77
N10	26464	25432	24707	26688	0.76	0.72	0.75	0.76

Tables 5.4 and 5.5 show the RMSE and KGE for only high and low water, respectively. During high water, network N01 performs best regarding the RMSE, except in parameterization strategy PS YG. KGE indicates contrasting tendencies in which PS GG and PS YP perform best with the densest network (KGE of 0.63 and 0.64, respectively) whereas PS YG exhibit the highest KGE (0.66) in the sparsest network (N10). The lowest RMSE and highest KGE is given by PS PP. Regarding low water, the sparsest network (N10) results in all parameterization strategies in the lowest RMSE and highest KGE.

Table 5.4: Root mean square error (RMSE) and Kling-Gupta efficiency (KGE) obtained for high water only.

	RMSE				KGE			
	PS GG	PS PP	PS YG	PS YP	PS GG	PS PP	PS YG	PS YP
N001	21663	19255	21758	20217	0.63	0.68	0.58	0.64
N01	20309	17677	19208	19302	0.61	0.71	0.63	0.64
N1	21688	18339	18996	21040	0.57	0.70	0.64	0.57
N10	23573	19984	19239	23968	0.50	0.65	0.66	0.49

Table 5.5: Root mean square error (RMSE) and Kling-Gupta efficiency (KGE) obtained for low water only.

	RMSE				KGE			
	PS GG	PS PP	PS YG	PS YP	PS GG	PS PP	PS YG	PS YP
N001	40549	45674	44875	42833	0.36	0.17	0.01	0.29
N01	34603	38647	38902	35314	0.42	0.36	0.21	0.41
N1	30588	33340	33160	30244	0.46	0.44	0.37	0.47
N10	29761	31269	30193	29729	0.48	0.47	0.47	0.48

5.3.2 Normalized water level at Obidos

The model schematizations capture the timing of the water levels better than the amplitude (Figure 5.9). In terms of water level amplitude, simulated high water level underestimates the observed one by around 1 m and the simulated low water levels overestimates it by around 2 m. For all parameterization strategies, the sparsest network (N10) reveals the largest water level amplitude. On the other side, the highest channel density leads to the smallest water level amplitude. The parameterization strategies PS GG and PS PP, in turn, generate also slightly larger water level amplitudes than PS YG and PS YP. The calculated RMSE yields a value of 1 m for each parameterization strategy in the sparsest network (N10) and 1.1 m, 1.2 m, 1.4 m, and 1.3 m for PS GG, PS PP, PS YG, and PS YP, respectively for the densest network (N001) (Table 5.6). In addition to Figure 5.9, the same results are plotted with respect to the network densities in Figure B.2 in Appendix B.2.

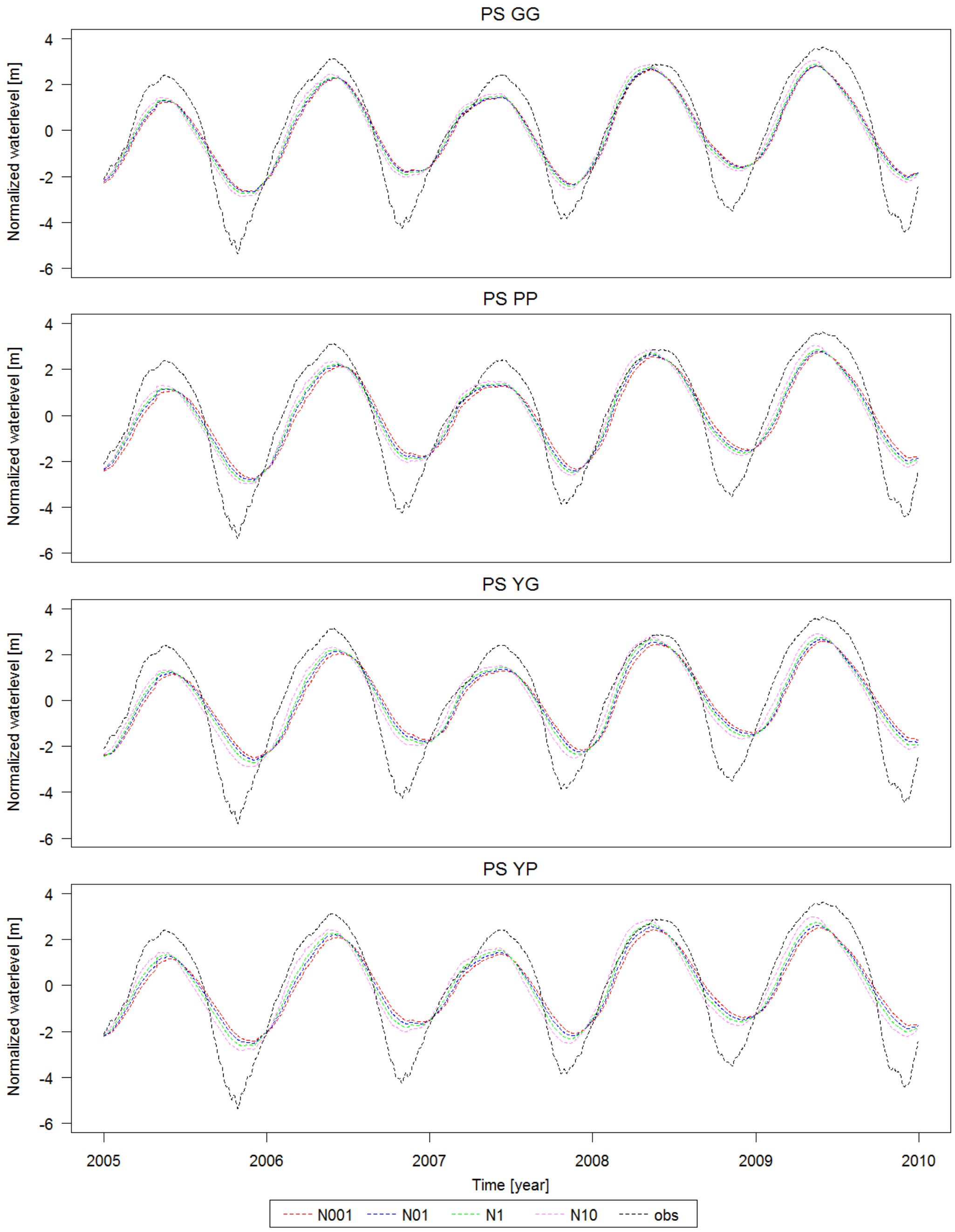

Figure 5.9: Observed and simulated normalized water levels at Obidos.

Table 5.6: Root mean square error (RMSE) obtained to evaluate normalized water level.

	PS GG	PS PP	PS YG	PS YP
N001	1.1	1.2	1.4	1.3
N01	1.1	1.1	1.3	1.2
N1	1.0	1.0	1.2	1.1
N10	1.0	1.0	1.0	1.0

5.3.3 Inundation extent

Figure 5.10 and Figure 5.11 illustrate simulated and observed inundation extents for the time period May to July 2009. The networks N001 and N01 with the respective parameterization strategies are plotted in Figure 5.10. The remaining two networks, N1 and N10, are given in Figure 5.11. The densest network leads overall to the highest hit rates, ranging between 78% and 89%. Not only the hit rate but also the false alarm rate is largest in this river network. Hit rates and false alarms continuously decrease with a decrease in channel density. The critical success rate ranges for all schematizations between 40% and 46%. Inundation in the upstream area is omitted in the sparser networks (e.g. N1 and N10) leading on one side to a low hit rate, but on the other side also to a minimized false alarm rate. The best agreement between simulation and observation is achieved by P01 having a critical success rate of 46.38%. The other parameterization strategies in this network, G01, YG01, and YP01, perform only slightly poorer exhibiting a critical success rate of 45.88%, 45,51%, and 46.09%, respectively. Simulated inundation resulting from the bathymetry parameterizations in N001 and N01 varies spatially most notably in the northern and western part, that is the upstream area of the study area. Hardly any differences are visible among all schematizations for the Lower Amazon and its mouth. Inundation between the channel networks varies mainly due to the existence or non-existence of river branches. In some cases, for instance, in G001 and G01 at 4.5°South and 66°West, inundation extent varies also for river branches both networks have in common. Visual inspection indicates that PS YG leads overall in all network extents to the largest amount of flooded area.

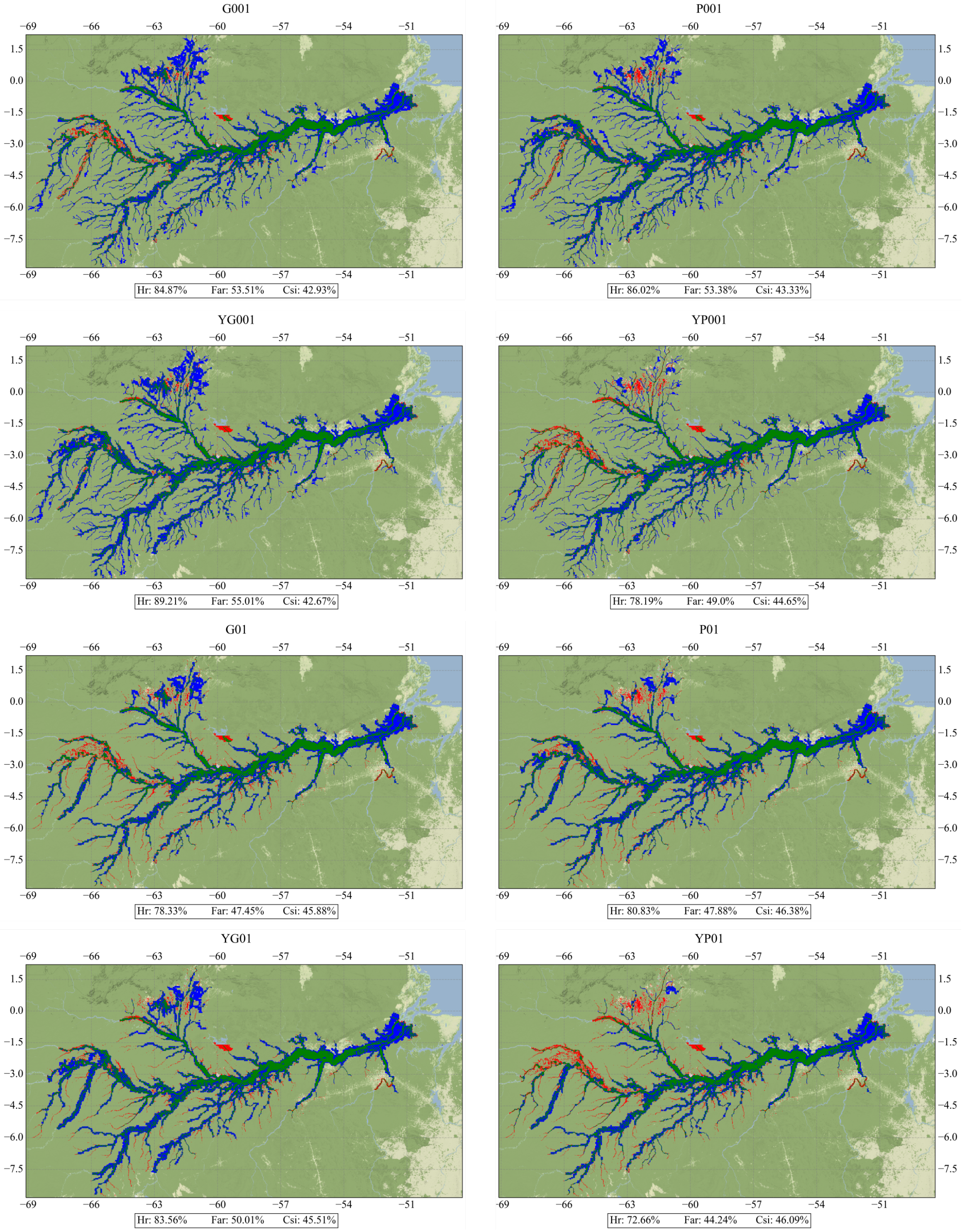

Figure 5.10: Simulated and observed inundation extent (May to July 2009) where inundation occurred in both maps (green cells), only in DFM (blue cells), or only in benchmark map (red cells). Network N001 and N01 with the respective bathymetry parameterizations are shown in this graph.

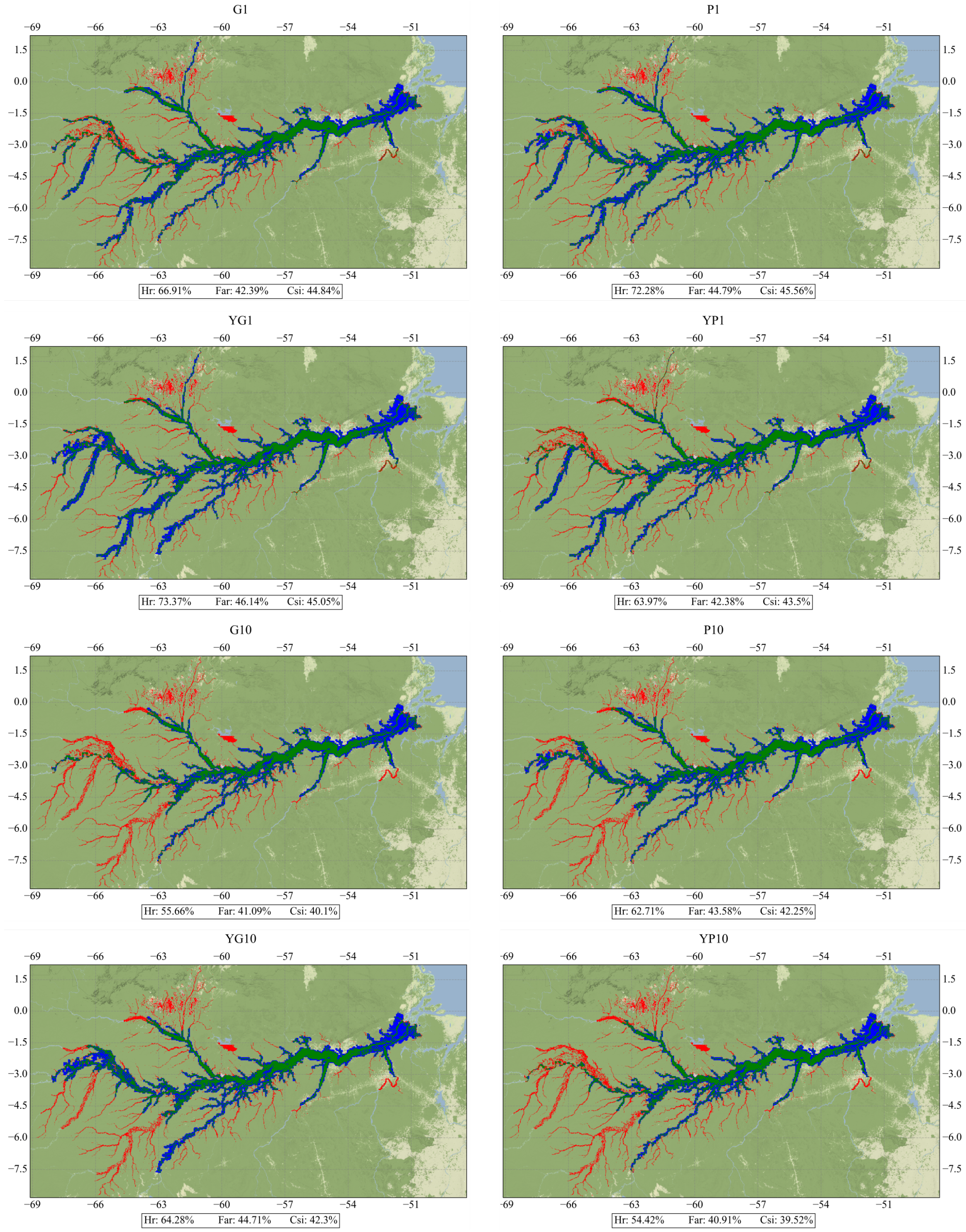

Figure 5.11: Simulated and observed inundation extent (May to July 2009) where inundation occurred in both maps (green cells), only in DFM (blue cells), or only in benchmark map (red cells). Network N1 and N10 with the respective bathymetry parameterizations are shown in this graph.

5.3.4 Model run times

All simulations were performed in a Linux environment with an Intel i7-4790 core at 3.90 GHz and 16 GB memory. The run times for all simulations are given in Table 5.7. The sparsest network, having the fewest 1D computational nodes, results in the fastest run times of around 18 h and 19 h for the respective parameterization strategies. The run times increase steadily with an increase in channel density as a consequence of a higher amount of computational nodes in the 1D network. The densest network N001 leads to the longest run times ranging between 24 h in PS YP and 29 h in PS YG.

Table 5.7: Run times (in hours) for each schematization.

	PS GG	PS PP	PS YG	PS YP
N001	26	28	29	24
N01	25	24	26	23
N1	20	21	22	20
N10	18	18	19	18

Chapter 6

Discussion

The 1D channel network extent as well as the bathymetry parameterizations are likely to impact the simulation of flood-relevant parameters. This is because the former changes travel times since river channels exhibit smaller friction forces than the floodplain. The latter defines whether inundation occurs (Getirana et al., 2012) and probably modifies the friction influence within the channel as a result of different river widths and depths as well. The present study investigates how sensitive the model is to different 1D channel network densities and bathymetry parameterizations in terms of overbank storage and the consequent flood wave propagation and attenuation. Moreover, the study explores which 1D channel network density and parameterization strategy results in the most accurate model performance with regard to river discharge, water level and inundation extent when compared with in-situ measurements and remote sensing observations, respectively. Last, the possible trade-off between computational costs and model accuracy in terms of discharge, water level, and inundation extent is investigated.

6.1 Sensitivity analysis

The sensitivity analysis was performed by using two different initial water conditions in the model domain which can be considered as two extreme states at both ends. In the first case, that is starting the simulations with initial water depths in the 1D/2D model domain, an extremely wet floodplain environment is represented where local topographic depressions are transformed into lakes. The results from these model runs look near-identical suggesting an insensitive hydrologic response at the downstream observation location, especially to the 1D river network. The second case, in turn, describes the opposite situation in which the floodplain as well as part of the river channels are completely dry. This yields different hydrologic responses due to the implemented schematizations and thus introduces model sensitivity. Both extreme states, completely wet and dry, do not reflect the Amazonian conditions in a realistic manner and the real conditions are more likely to range between these two extreme states. However, the results show that with different initial conditions, be it in the 1D channel or 2D floodplain, the system is likely to respond in a different way to a hydrological event.

6.1.1 Wet conditions (i.e. model runs with initial water depths)

6.1.1.1 Discharge and water level at observation location

Further analysis of the results shows that the floodplain of the Amazon River is completely flooded from the early beginning of the rainfall event until the end of the simulation period. This is the case for all parameterization strategies. This fact is likely to impact the possible influence of the 1D networks and river bathymetries on the hydrological response because floodplain and channel act as a whole and the influence of river bathymetry in terms of channel storage and friction is hampered.

6.1.1.1.1 1D network density

The resulting flood wave propagation and water level seem to be insensitive to the different 1D network extents. Only marginal variations in the flood hydrographs are distinguishable. The densest network responds more rapidly to the rainfall event than the other channel networks and leads in case of PS GG also to a higher peak discharge. Regarding the parameterization strategies, PS YG and PS YP, the peak discharges in the densest network (N001) are slightly attenuated and delayed. The cumulative discharges, however, for all parameterization strategies are largest in the densest network (N001). The attenuated peak discharge in the densest network (N001) in PS YG and PS YP could be caused by inundation in the upstream area due to local variations in channel bathymetry. The reduced water level amplitude in PS YG and PS YP with increased 1D channel density supports this assumption. Besides the all-time inundated Amazon River and its floodplain, another possible explanation for the almost insensitive outcomes is the initial water depths on the 2D floodplain (Figure 4.9). Because of the initial water depths on the 2D domain, the floodplain acts like a channel where friction is diminished and topographic depressions filled. Consequently, the hydrologic response at the observation location (obs-loc) yields near-identical flood hydrographs.

6.1.1.1.2 River bathymetry

The findings suggest that the bathymetry parameterizations affect the hydrologic response in the study area slightly larger than the 1D network extents. During the simulation period, a cumulative discharge of 1.78 x 10^{12} m^3 is drained by PS YP, 1.76 x 10^{12} m^3 by PS YG, 1.70 x 10^{12} m^3 by PS GG, and 1.65 x 10^{12} m^3 by PS PP for the densest channel network (N001). This order reflects the differences in channel storages (Table 5.2) whereby greater channel storages cause more water to be accumulated and transported within the channel. The river geometry derived from PS YG and PS YP, however, exhibit a larger wetted perimeter, that is the interfacial area between water and the bed and walls of the river, than PS GG and PS PP which in turn may lead to a deceleration of the flood wave propagation in PS YG and PS YP. Channel friction is highest at the river bottom and walls (i.e. wetted perimeter) and thus, water tends to be stored within the channels in the parameterization strategies PS YG and PS YP. This may explain the smaller peak discharge when compared with PS GG and PS PP (Figure 5.3). One might expect that due to narrower river widths and/or shallower river depths, and hence also smaller channel storages in PS GG and PS PP, more flooding occurs which delays and attenuates the flood wave as well. This, for instance, was encountered in the sensitivity analysis performed by Yamazaki et al. (2011) who showed that indeed a time delay of the flood peak as well as a reduced discharge fluctuation occurred when river depth was shallower and river width narrower. The same was also found by Paiva et al. (2013a). Figure 5.4 in Chapter 5.2.1.2 illustrates a smaller water level amplitude for PS YG and PS YP than for the other two parameterization strategies. A reduced water level amplitude indicates an attenuation of the flood wave. The reason for this attenuation could be attributed to local inundation in upstream areas and higher channel frictions. The findings between this study and the ones obtained by Yamazaki et al. (2011) and Paiva et al. (2013a), however, cannot be compared directly in that Yamazaki et al. (2011) and Paiva et al. (2013a) altered the river parameters separately and, more importantly, homogeneously (i.e. the river widths for the entire network are either increased or decreased) whereas in this study different parameterization strategies are used which leads to heterogeneity among them (i.e. river widths in PS YP are overall larger than for instance in PS PP, but may locally be smaller as well).

The results in Chapter 5.2.1.1 also indicate that the differences in the hydrological response between the river bathymetries are minimal for the sparsest network (N10). Network N10 represents the main stems of the Amazon River and its major tributaries. These river branches exhibit the largest drainage areas in the watershed and therefore the largest water volumes are available because rainfall is distributed spatially uniform. The enormous water volumes occurring in the Amazon River may diminish the influence of channel friction, as noted by Sioli (1984). In addition, the difference in channel storages between the parameterization strategies is lowest for the sparsest network (N10), ranging between 341 km^3 and 567 km^3 (Table 5.2) which may also explain the minimised differences among the parameterization strategies.

6.1.2 Dry conditions (i.e. model runs without initial water depths)

6.1.2.1 Discharge and water level at observation location

6.1.2.1.1 1D network density

The model runs with dry floodplain conditions reveal that the hydrologic response in the study area changes with different 1D channel densities. The mean relative difference indicates the mean increase of the flood hydrographs from the densest network over the sparsest network. It describes the differences between paired members of each group (i.e. the differences between the discharges from N001 and N10 at each time step). The comparison between the densest (N001) and sparsest (N10) network yields a mean relative difference of 94%, 81%, 72%, and 80% for PS GG, PS PP, PS YG, and PS YP, respectively. The cumulative discharge resulting from the densest network (N001) increases in PS GG by 64%, in PS PP by 59%, PS YG by 53%, and PS YP by 48% over the cumulative discharge from the sparsest network (N10). If more channels are present, more water can be accumulated and conveyed downwards. The larger amount of discharge results subsequently in higher water stages as well. In addition, the densest network leads to a quicker flood wave propagation in which the flood peak arrives approximately one month earlier than compared with the sparsest network. These findings follow the GIUH (Geomorphologic Instantaneous Unit Hydrograph) theory (Rodríguez-Iturbe and Valdes, 1979) which implies that the network structure and hence the network path lengths result in different hydrologic responses due to different travel times (Rinaldo et al., 1991; Saco and Kumar, 2004; Pattison et al., 2014). This is because of the lower friction (Manning's n 0.03) of the river channel compared with the one of the floodplain (Manning's n 0.08). With a higher channel density, the flow paths for water on the 2D floodplain are likely to be shortened as more channels exist in the study area and once it reaches a channel it will flow downstreams at a higher rate.

The results in Figure 5.5 not only highlight the differences in flood wave propagation among the network densities but also indicate the variations in the cumulative discharge volumes. These findings demonstrate that the cumulative discharge at the observation location (obs-loc) increases with an increase in network density. In the absence of 1D channels, more water is restrained on the 2D floodplain due to topographic depressions, whereas the drainage in these depressions is enabled when channels are present. This finding agrees well with other studies investigating the impact of 1D channels on water volume conveyance (Hoch et al., 2017a).

6.1.2.1.2 River bathymetry

The model runs without the restart files result in more pronounced changes among the parameterization strategies. This is mainly due to the empty dead storages in the channels which are subsequently filled. The parameterization strategy exhibiting the lowest channel storage in the respective 1D channel network (PS GG in N001, and PS PP in N01, N1, and N10) yields also the highest cumulative discharge. As a result of water storage in the channels owing to dead storages, our ability to further investigate the possible impacts of bathymetric input on the hydrologic response is limited.

6.1.3 Limitations

To our knowledge, no other study explored yet the effects of 1D network extents on the hydrologic response, therefore excluding the possibility to compare the obtained results with existent literature. The sensitivity of the model results to the 1D channel networks might be influenced by the quality of the DEM representing the floodplain topography and the degree of modification the DEM experienced (e.g. alteration of elevation values by a pit removal algorithm). Misrepresentation of elevation values in the DEM may hamper the water supply from the floodplain to the river channel and could lead to a more approximated effect (in terms of the hydrologic response) between the different 1D networks if water flows besides the channel on the floodplain. The primary reason for the different hydrologic responses resulting from the network extents is the varying friction coefficient between channel and floodplain in which the latter is typically larger. Hence, by using other friction values than the ones used in this study, the hydrologic response is likely to change as well. The channel friction is mainly determined by the type and size of the material composing the river bed and walls as well as by the channel shape (Arcement and Schneider, 1989). Not only the the vegetation, but also the physical shape impact the roughness coefficient of the floodplain. As noted by Werner et al. (2005), using a single friction coefficient for the entire floodplain introduces a higher model sensitivity than when spatially different friction coefficients are implemented. DFM allows to specify a single friction coefficient only for the floodplain. The used floodplain friction has consequently a large influence on the performed sensitivity analysis. The spatially uniform floodplain friction of 0.08 in this study is slightly lower than the floodplain friction coefficient of 0.10 applied for instance by Wilson et al. (2007), Yamazaki et al. (2012a), and Baugh et al. (2013). Rudorff et al. (2014) used values of 0.14 and 0.10 for the vegetation classes forest and scrub, respectively. By applying a higher floodplain friction coefficient than 0.08, the differences in the hydrologic response may become even more pronounced. The channel friction of approximately 0.03, in turn, is widely used among the studies in the Amazon Basin (Trigg et al., 2009; Yamazaki et al., 2011; Baugh et al., 2013; Rudorff et al., 2014; Hoch et al., 2017a). The potential influence of river bathymetry on the hydrologic response in terms of friction depends largely on the friction value itself. Paiva et al. (2013a) and Yamazaki et al. (2011) showed that changes in the channel friction affected simulated discharge, flooded area, and water depth. A larger friction value probably increases also the impact due to the river bathymetries. The Amazon River and its floodplain, however, are consistently flooded during the simulation period and the influence of channel friction becomes less significant due to increased water depths. In this sensitivity analysis, water is spatially supplied to the entire 2D floodplain which in turn limits to test the model sensitivity to inundation extent.

6.2 Accuracy analysis

Simulated discharges produced by all schematizations perform fairly well when compared against in-situ observations. Despite the overall good model performance, the diverse schematizations yield slightly different validation outputs. As already mentioned in Chapter 4.3.2.2, water levels were normalized in order to maintain a certain degree of comparability between observed and modelled values. The simulated water levels capture the timing reasonably well but underestimate the water level amplitude. Simulated water levels seem to be almost insensitive to both 1D channel network density and river bathymetry. Inundation pattern, in turn, varies with both, 1D channel network density and bathymetry.

6.2.1 Validation of discharge

6.2.1.1 1D network density

Regarding simulated and observed discharge at Obidos, the RMSE increases with an increase in channel network density (Table 5.3). The hydrograph resulting from the sparsest network (N10) hence fits the observed hydrograph better. KGE shows no clear trend between the network densities in which the best fit is performed by network N1 for all parameterization strategies. Overall, the high water flows of the Amazon River are better captured by the schematizations than the low water flows during the dry seasons in which discharges are overpredicted. The overprediction of low water flows may be attributed to two reasons. First, DFM lack to simulate evaporation (and infiltration) and hence is likely to overpredict discharge especially in the dry season in which evaporation rate is highest (also noted in Hoch et al., 2017a). Second, water on the floodplain is not able to fully drain back to the channel. The floodplain, in fact, stays completely inundated during all times (Figure 6.1). This phenomenon is also observed in the sensitivity analysis. Two years after the synthetic rainfall event, the floodplain is still inundated (∼5 m water depth) indicating an extremely slow drainage.

A similar problem was encountered by Wilson et al. (2007) and Rudorff et al. (2014) as a result of small misrepresentation in the DEM. Some parts of the floodplain become hydraulically disconnected from the river channels during low water resulting in a patchwork of small lakes and channels that drain slowly back to the river (Wilson et al., 2007). In the performed accuracy analysis, the floodplain during low water, however, is completely flooded and thus a disconnectivity of the floodplain to the river channel can be excluded. The problem may lie in a poor representation of the delta region in terms of topography on the one hand, and river bifurcation on the other hand. The former is introduced by irregularities in the SRTM DEM leading to over-elevated areas and hence hindering water on the floodplain to flow out of the system. The Amazon delta consists of a complex network of bifurcating river branches which allows the vast water volumes to be allocated to multiple river streams. The complex bifurcating river system in the delta is in this study represented by one single main stem which needs to drain the immense water volumes occurring at the mouth of the Amazon River. Not accounting for river bifurcation in the delta region possibly cause water to be dammed and hence affecting upstream areas as a result of backwater effects, as noted in Yamazaki et al. (2014b). Yamazaki et al. (2014b) found, although for the Mekong River basin, that around 50% of water is transferred from the main stem to surrounding bifurcation channels in the delta. By not including bifurcation channels, water levels in the main stem were overestimated and the hydrodynamics of the wider river basin were affected due to backwater effects. These two factors may generate a bottle-neck effect whereby water is obstructed to flow out of the system. This would explain the all-time inundated floodplain and the very slow drainage which in turn is also indicated by extremely slow flow velocities of around 0.25 m s^{-1} during high water in the Lower Amazon. Values of 0.5 - 1.0 m s^{-1} at low water and 2.0 m s^{-1} at high water are stated in literature for the Lower Amazon (Sioli, 1984).

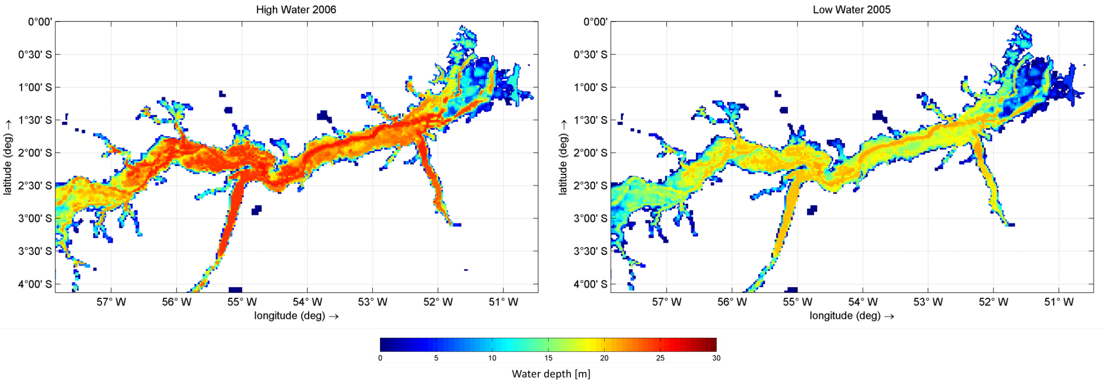

Figure 6.1: Floodplain water depths during high water (June 2006) and low water (December 2005) for the network with the highest channel storage (YP001). Shown here is the floodplain of the Lower Amazon and the delta region.

As shown in Figure 5.8, the densest network (N001) leads to higher peak discharges as well as higher discharges during low water. By comparing the entire simulated hydrographs (i.e. high and low water), the sparsest network (N10) results consequently in a better fit (indicated by the lower RMSE in Table 5.3) because low water flows are less overpredicted than by the densest network (N001). This is in line with the findings in Table 5.5. The sparsest network (N10) overpredict the low water flow less than the denser networks and thus results in the best model performance regarding RMSE and KGE. Since water is added from PCR directly to the 1D channel network in DFM, the channel density has an impact on the allocation of the available water volumes in DFM. During high water, denser 1D channel networks show a better agreement in both RMSE and KGE (for PS GG, PS PP, and PS YP in Table 5.4) indicating that when water inputs to DFM are largest (i.e. during high water) the channel density play an important role in regulating river hydrodynamics.

The densest network (N001) produces in all parameterization strategies higher discharges during both high and low water. In addition, the peak in the N001 arrives in general a bit later (in the range of days). This could be attributed to the longer flow paths and hence travel times in the densest network (N001). The four implemented network extents receive diverse water volumes from PCR which are in total 4.59 x 10^{13} m^3, 4.47 x 10^{13} m^3, 4.36 x 10^{13} m^3, and 4.34 x 10^{13} m^3 in N001, N01, N1, and N10, respectively. Expressed as percentage, network N1 receives 0.5%, network N01 3.0%, and network N001 5.8% more water than network N10. Thus, as more water is supplied to the densest network, also more water can be drained than by the other networks. Water from PCR is supplied directly to the 1D network which means that in case of the sparsest network (N10) water stays for a longer time in PCR as a larger spatial distance needs to be covered until the coupled PCR-DFM cells are reached (explained in Chapter 4.3.2.1). Consequently, due to the prolonged retention time in PCR, a higher amount of water may be lost by evaporation and infiltration processes. This could explain the decreasing water input into DFM when using a sparser channel network.

6.2.1.2 River bathymetry

Similar to the 1D networks, the resultant hydrographs obtained from various river bathymetries look near-identical. The RMSE in Table 5.3 indicates that the different river bathymetries have a minor impact on the simulated discharge and that the 1D networks have a greater influence. Contrary to this, obtained KGE implies that river bathymetry affects the model outputs stronger than the 1D networks. Parameterization strategy PS PP exhibits the lowest KGE (0.69) whereas both PS YG and PS YP result in the highest KGE (0.77). Compared with the other parameterization strategies, PS PP leads in all network extents to the lowest peak discharges. In fact, PS PP shows the smallest discharge amplitude which is probably caused by larger inundation in upstream areas due to minimized channel storage capacity. Discharge is highly dependent on the spatial and temporal occurrence of precipitation, evaporation processes and runoff generation (Yamazaki et al., 2012b). PCR accounts for these hydrological processes and plays thus an essential role in regulating river discharge. River bathymetry defines weather river overflow may occur (Getirana et al., 2012), but as a result of the hampered floodplain drainage of the Amazon River (discussion in Chapter 6.2.1.1), river channel and floodplain are consistently inundated. This, of course, diminishes the potential influence of river bathymetry on the hydrologic response since channel storages are filled up and friction minimized. The flow velocities at Obidos resulting from the bathymetry parameterizations differ only marginal around 0.03 m s^{-1}. PS YP and PS YG yield slightly higher flow velocities than PS PP and PS GG. During high water, PS PP leads overall to the lowest RMSE (17,677 m^3) and the highest KGE (0.71). Parameterization strategies PS GG and PS YP perform best at low water (Table 5.5). Regarding the model skill at high water, the effect of channel morphology dominates over the 1D network. The influence of the 1D channel network on the model output, however, dominates during low water.

6.2.2 Validation of water level

6.2.2.1 1D network density

Since simulated water levels at Obidos showed a significant overprediction compared with observed stages, possibly due to elevation irregularities on the one hand and the hampered floodplain drainage on the other hand, observed and simulated water levels were normalized to ensure comparability in terms of amplitude and timing. Normalized water levels simulated by all 1D networks underestimate the observed amplitude. The mean deviation to the observed water levels varies between 1.0 m and 1.4 m (RMSE in Table 5.6). The network densities result in very similar water levels and differ in the range of centimeters. The temporal variation of water stages seems to be captured fairly well by the schematizations. The sparsest network (N10) exhibits the largest water level amplitude among the 1D networks. A lower water level amplitude suggests that water is possibly attenuated as a result of flooding in the upstream areas. This is reasonable due to two reasons. First, water from PCR is supplied over a larger area in the densest network (N001) in which flooding and hence attenuation may occur because of local variations in river bathymetry. Second, the total water volume from PCR is basically added to one single river branch in N10, although this is the main stem, which is likely to inundate the floodplain of the main stem as well and probably with a greater extent. Since the floodplain of the Amazon River is unable to drain, the increase in water depth on the floodplain may not cause such a large attenuation effect in that friction becomes less pronounced with larger water depths. The simulated water level amplitude would further be enlarged and hence closer to the observed amplitude, if water on the floodplain is able to drain. As noted by Yamazaki et al. (2012b), water level is strongly affected by local processes and characteristics such as channel bathymetry, river bed slope as well as infilling and draining of floodplains and hence may be less sensitive to different 1D channel networks.

6.2.2.2 River bathymetry

Water levels are locally affected for instance by river bathymetry (Yamazaki et al., 2012b). The normalized water stages, however, indicates an almost insensitive response towards the varying river bathymetries. Not only bathymetry but also filling and drainage of the floodplains play an important role in regulating water stages. Because the floodplain at Obidos is not able to drain, this consequently leads to almost identical water levels. The lowest RMSE (1.0 m) is obtained in all parameterization strategies (Table 5.6). On the other end, PS YP generates the highest RMSE (1.4 m) in the densest network (N001).

6.2.3 Validation of inundation extent

6.2.3.1 1D network density

Network N01 results overall in the best model performance with respect to the critical success rate between simulated and observed inundation extent. A higher hit rate is scored by the densest network (N001) but this is accompanied by a higher false alarm rate as well. More channels exist and hence the probability to hit an observed inundated cell is maximized as well as the probability to erroneously predict flooding. PS YG in the densest network (N001) generates both the highest hit rate (89.2%) and highest false alarm rate (55.01%). With a decrease in channel density, the chances to wrongly predict a flooded cell becomes smaller including the probability to miss an actual flooded cell. PS YP in the sparsest network (N10) yields the lowest false alarm rate (40%). This is because fewer areas are inundated and hence the chance to erroneously predict inundation is minimal. The same schematization, however, produces also the lowest hit rate (54.42%) and yields the lowest critical success rate (39.52%). Interestingly, inundation occurs in the upstream part in the northern region (Negro River) of the sparsest network (N10) even though there are no channels present in this upper region. This is facilitated owing to the excessive water stages occurring in the entire Amazon River.

Water from PCR is supplied to DFM by dividing the available water volumes from the coupled PCR cell over all available river branches (computational nodes) within the specific PCR cell. A higher channel network density is likely to have more river branches within a specific PCR cell and water volumes are thus collocated to more branches. If only a few river branches exist within the PCR cell, all available water volumes will be added to these few branches. For example, if all available water volumes are added to one single river branch, inundation at this specific river branch is more likely to occur as if the same water volumes are divided over multiple river branches. This in turn may cause inundation in the other river branches but not in the specific river branch in this example. Thus, the 1D channel density occurring within a PCR cell has an impact on whether inundation occurs in a specific river branch because it defines how much water will be added to this river branch (seen for instance in Figure 5.10 the the western part of the study area in G001 and G01).

6.2.3.2 River bathymetry

Even though the critical success rate among the parameterization strategies in the respective river networks differs only by 2% or 3%, it is visible that due to variations in river bathymetry different areas are flooded. The flood extents among the bathymetry inputs disagree most notably in the northern part and western part of the study area. Not only river bathymetry but also the topography influences the flood extent since it describes the flow paths over the floodplain. Further differences in flood extent due to river bathymetries might emerge if a finer model resolution is used which provides more topographic details. Based on the critical success rate, P01 shows the best model performance (46.38%).

6.2.3.3 Limitations

The coarse spatial model resolution (up to 5 km) limits the ability to simulate accurately overbank flow as detailed topography is required which cannot be represented by such coarse grid cells (Yamazaki et al., 2012b). The existing trade-off between spatial model resolution and computational effort in large-scale model applications is well-known (Savage et al., 2016). Implementing a finer spatial model resolution consequently leads to a higher number of calculations and reduced model time steps (required to ensure numerical stability) and therefore to excessive computational costs especially for multi-year simulations (Savage et al., 2016). Moreover, by not including river bifurcation in the delta region, the overall model performances in terms of flood extent are further deteriorated. In DFM, the entire river delta is flooded which leads to a substantial amount of erroneously flooded cells which impacts the binary inundation measures false alarm rate (increased) and critical success rate (decreased). The comparison between the schematizations, however, is not affected by this since the delta region is inundated in all schematizations. The used benchmarking inundation data, having a native spatial resolution of 30 m (Landsat), was upscaled to a cell size of 1 km using the nearest neighbour method. Simulated flooded extent emanating from a much coarser resolution (up to 5 km) was downscaled to the same raster resolution of 1 km in order to apply the binary inundation measures. The validation data includes also lakes (e.g. at 1.5°South, 60°West) which also impact the scores of the hit rate and critical success rate. The model performance in terms of inundation extent cannot be compared with other studies as they are either on a smaller spatial model resolution (∼100 m Rudorff et al., 2014), or are non-existent for the Amazon Basin.

6.2.4 Run times

The run times increase with the usage of higher channel network densities. This is because more 1D computational nodes exist which expands the number of calculations. The run times might be further influenced by more computationally expensive interaction between the coupled 1D/2D cells in DFM (Hoch et al., 2017b). The model run with the densest network (N001) lasts between 6 h and 10 h (i.e. 33.3% and 55.6%) longer than the runs with the sparsest network (N10). Variations in model run times among the parameterization strategies may emerge for instance through diverse flow velocities affecting computed model time steps. In terms of validating discharge and water level results, the accuracy analysis suggests using a sparse 1D network (e.g. N1, N10) in which model run times and thus computational costs are reduced. Considering the multi-year simulation of 6 years (including one spin-up year) resulting in run times of the order of a day, there may be a potential to implement a finer model resolution than the one used in this study. To minimize the increased computational effort as a result of a finer model resolution, the simulation period could be shortened.

6.2.5 Limitations

So far, it remains ambiguous whether the overlapping part in DFM between 2D cell and 1D computational node has an impact on the drying and wetting process of the 2D cell and on water exchange between them as the cell areas are double counted. Once a 2D cell in DFM is flooded it will remain in this state and no drying (0 m water depth) takes place. According to Neal et al. (2012), floodplain connectivity enabled through small channels improved simulation accuracy in terms of water level simulation, wave propagation speed, and inundation extent. This cannot be tested in this study as floodplain is consistently inundated which results in uniform water stages and inundation extents in the Amazon River among the different 1D network densities.

Chapter 7

Conclusion

This study assessed how different 1D channel network densities and river bathymetries originating from various parameterization strategies affect the outputs of hydrodynamic modelling. The Amazon River was used as the test side. First, the model sensitivity in terms of flood wave propagation and attenuation, and water level to the diverse schematizations was analyzed. To this end, DFM run standalone and model internal boundary conditions were set up in order to create a synthetic rainfall event. Second, DFM was spatially coupled to PCR from which daily water volumes were supplied to the 1D network. This was done by dividing available water volumes from a PCR cell over the computational nodes of the 1D network lying within the specific PCR cell. The period between 2005 and 2009 was subsequently simulated and the agreement between the model outcomes and observations evaluated. In addition, run times due to the different 1D channel network extents were compared to investigate the trade-off between computational costs and output yield.

7.1 Model sensitivity

The sensitivity analysis was performed by using two different initial conditions in the 1D/2D model domain, that is wet and dry conditions. The relevance of the network extent and the river bathymetry on the hydrologic response is likely to change with varying initial conditions. The findings suggest an almost insensitive model output in which flood wave propagation and attenuation, and water level differed only marginal with the implemented 1D network extents. This is probably due to the initial water on the 2D domain which reduces the friction difference between channel and floodplain. The river bathymetries were found to have a slightly larger impact. More water is transported downstreams if the channel storage capacity is larger. The variation among the outputs resulting from the bathymetry parameterizations becomes more pronounced with a higher channel network density. This is because flow path lengths are larger and friction forces and local inundation thus are able to act on a greater area. Moreover, we found that the parameterization strategies, PS YP and PS YG, leads to a larger flood peak attenuation than PS GG and PS PP. This is possibly attributed to a higher friction influence within the channel as a result of a larger wetted perimeter and inundation due to local variation in river bathymetry.

Flood wave propagation and attenuation, and water level were found to be sensitive to the 1D network density in case of dry floodplain conditions. Conveyed discharge with the densest network increase by more than 50% when compared with the sparsest network. With a higher 1D channel extent, more water is accumulated and conveyed downstreams which results in a higher peak discharge as well. River channels enable water in topographic depressions to drain while water remains in these areas without the presence of channels. A higher channel density results additionally in a faster hydrologic response in terms of flood wave arrival time. In the densest network, the flood peak arrives one month earlier than in the sparsest one. Since different water volumes are stored in the river channels due to dead storages originating from the diverse river bathymetries, the resulting differences between the hydrologic response cannot be attributed to friction and inundation processes only. We expect, however, that especially for low water the friction influence within the channel will take on greater significance. A single uniform friction coefficient for the channel and floodplain was used in this study. Hence, the obtained results are bound to the used values and may thoroughly change with other friction values. A higher or lower floodplain friction coefficient may alter the model's sensitivity regarding the hydrologic response. Therefore, the obtained results cannot be translated directly to other river basins as the friction coefficients of the floodplain but also from the channel certainly change.

7.2 Model accuracy

In the second part of this research, the agreement between simulations and observations in terms of discharge, water level, and inundation extent was analyzed. The RMSE increases with an increase in channel network density. No clear trend was given by the second measure, KGE, in which network N1 performed best. The fact that the sparser networks tend to produce a better agreement between observed and modelled can be attributed to the better performance of the sparser networks during low water. Since DFM lack to simulate evaporation (and infiltration), discharge is likely to be overpredicted during the dry season. Compared to the densest network, the sparsest one leads to lower discharges during both high and low water. Hence, for the overall performance of simulated discharge, the densest network is consistently closer to the observed low water discharge than the denser networks. This is confirmed by applying the measures RMSE and KGE separately to only high and only low water discharges. The findings demonstrate that the sparsest network performs best during low water whereas the denser networks tend to show a better agreement during high water. The differences in the hydrographs among the 1D networks may arise due to different water inputs from PCR as more water is supplied to the densest network. The flow paths in PCR are longer in case of a sparse network because the spatial distance to the coupled PCR-DFM cells becomes larger and thus water is exposed to infiltration and evaporation in PCR for a longer time than when PCR is coupled to the densest network. Hence more water is supplied to the densest network and more water is able to drain through the network. In this sense, the hydrologic response in terms of discharge seems to be driven primarily by water input from PCR.

With respect to river bathymetry, the overall best performance regarding simulated discharge is obtained by the parameterization strategies PS YG and PS YP (KGE 0.77). During high water, however, PS PP performs best. This study shows that different bathymetry parameterizations lead to different model outcomes. The most important limitation of this study lies in the inability of water to drain from the floodplain and out of the system. We speculate that misrepresentation of elevation emanating from the SRTM DEM and the omission of river bifurcation in the Amazon delta might be responsible for the hindered water drainage. This fact may well offset the possibly distinct occurring model outputs due to the implemented schematizations and needs to be investigated in future studies. Since the Amazon River is consistently flooded, river bathymetry plays only a minor role where channel friction influence is hampered as a result of the large water depths. This is in accordance with the simulated water levels at Obidos which indicated to be excessively high and needed to be normalized in order to compare them with in-situ measured water levels. All schematizations capture the temporal variation in water level fairly well but underestimate the water level amplitude as a possible result of hampered floodplain drainage. The differences among the network extents and among the river bathymetries are consequently marginal.

The validation of the flood extent demonstrated that both 1D network density and river bathymetry change inundation patterns in the study area. Despite the fact that all schematizations yield similar critical success rates ranging between 40% and 46%, inundation varies spatially due to the differences in river bathymetry on the one hand but also since different water volumes are transferred to the 1D network from PCR on the other hand. Daily available water volumes from a PCR cell are divided over the computational nodes of the 1D network in DFM. Hence, the channel density within a PCR cell defines whether the available water volumes are split over a large number of river branches or only a few. The amount of water added to a certain river branch has a determining influence on whether overbank flow may occur.

The coarse model resolution used in this study presents another major limitation especially in terms of simulating and validating inundation extent. A precise prediction of flooded extent is not able on such a coarse scale since detailed topography is required to accurately describe overland flow. As a result of the large grid cells, flooded area is likely to be overestimated by the model.

The run times among the schematizations differ in the order of hours. Yet, the findings indicate that a sparser network results in a better performance regarding overall discharge simulations (low RMSE, high KGE) in which the run times are minimized as well. Contrarily, an intermediate network density is favourable in terms of inundation extent but consequently causes an increase in computational costs. From a computational point of view, there is a potential to implement a higher model resolution and therefore include more topographic details which may improve model accuracy as a whole and may provide more in-depth insights about the role of the 1D network extent and river bathymetry. We found that for discharge, water level and inundation extent, different schematizations result in the best model performance. Hence, further research is needed in this regard in which more clarity could be established once water on the floodplain is able to drain properly.

Chapter 8

Recommendations

The current results lead to the conclusion that the 1D network densities have an impact on the hydrologic response. The 1D network extent should thus be represented as close to reality as possible. In case of the coupled modelling framework, inundation can only be modelled if river channels exist since water is added to them directly. This also evokes the need for a realistic 1D channel network representation.

This study shows further that different bathymetry parameterizations have an influence on the hydrodynamic modelling of floods. Therefore, the parameterization strategy needs to be chosen carefully and should represent the actual river bathymetry as accurately as possible. Regarding the simulation of discharge, water level and inundation extent, different bathymetry schematizations result in the best model performance. The analysis of the results revealed that there are certain issues which possibly limit the examination of the effect various river bathymetries have on the resultant model outputs. The same is true for the 1D river network extent as well. The floodplain of the Amazon River is not able to drain during low water as a possible result of misrepresentation of elevation values from the SRTM DEM and the omission of river bifurcation in the delta region leading to an obstructed drainage. We recommend that further research should be undertaken to tackle the encountered issues for instance by applying a river bifurcation scheme in the river delta and to investigate whether these issues considerably obscure the possibly occurring differences among the river bathymetries as well as 1D network extents.

Moreover, potential differences in the simulated inundation extent among the river bathymetries might disappear with a coarse spatial model resolution such as used in this study. By applying a finer spatial model resolution, more topographic details can be included which in turn might reveal spatially varying inundation patters along the river channels due to variations in river bathymetry. It would be thus beneficial to investigate whether greater variations in the inundation extent may occur among the diverse river bathymetries when a higher spatial model resolution is used. To this end, the multi-year simulation used in this study could be shortened in order to reduce computational efforts.

Bibliography

Ali, A. M., Solomatine, D., and Di Baldassarre, G. (2015). Assessing the impact of different sources of topographic data on 1-D hydraulic modelling of floods. *Hydrology and Earth System Sciences*, 19(1):631.

Alsdorf, D., Han, S.-C., Bates, P., and Melack, J. (2010). Seasonal water storage on the Amazon floodplain measured from satellites. *Remote Sensing of Environment*, 114(11):2448–2456.

Amir, M., Khan, M., Rasul, M., Sharma, R., and Akram, F. (2015). Hydrologic and hydrodynamic modelling of extreme flood events to assess the impact of climate change in a large basin with limited data. *Journal of Flood Risk Management*.

Andreadis, K. M., Schumann, G. J.-P., and Pavelsky, T. (2013). A simple global river bankfull width and depth database. *Water Resources Research*, 49(10):7164–7168.

Apel, H., Aronica, G., Kreibich, H., and Thieken, A. (2009). Flood risk analyses—how detailed do we need to be? *Natural Hazards*, 49(1):79–98.

Arcement, G. J. and Schneider, V. R. (1989). Guide for selecting Manning's roughness coefficients for natural channels and flood plains.

Arnold, J. G., Moriasi, D. N., Gassman, P. W., Abbaspour, K. C., White, M. J., Srinivasan, R., Santhi, C., Harmel, R., Van Griensven, A., Van Liew, M. W., et al. (2012). SWAT: Model use, calibration, and validation. *Transactions of the ASABE*, 55(4):1491–1508.

Asner, G. P. (2001). Cloud cover in Landsat observations of the Brazilian Amazon. *International Journal of Remote Sensing*, 22(18):3855–3862.

Bates, P. D. and De Roo, A. (2000). A simple raster-based model for flood inundation simulation. *Journal of hydrology*, 236(1):54–77.

Baugh, C. A., Bates, P. D., Schumann, G., and Trigg, M. A. (2013). SRTM vegetation removal and hydrodynamic modeling accuracy. *Water Resources Research*, 49(9):5276–5289.

Biancamaria, S., Bates, P. D., Boone, A., and Mognard, N. M. (2009). Large-scale coupled hydrologic and hydraulic modelling of the Ob river in Siberia. *Journal of Hydrology*, 379(1):136–150.

Bonell, M., Hufschmidt, M. M., and Gladwell, J. S. (2005). *Hydrology and water management in the humid tropics: hydrological research issues and strategies for water management.* Cambridge university press.

Bradshaw, C. J. A., Sodhi, N. S., Peh, K. S.-H., and Brook, B. W. (2007). Global evidence that deforestation amplifies flood risk and severity in the developing world. *Global Change Biology*, 13(11):2379–2395.

Bravo, J., Allasia, D., Paz, A., Collischonn, W., and Tucci, C. (2011). Coupled hydrologic-hydraulic modeling of the Upper Paraguay River Basin. *Journal of hydrologic engineering*, 17(5):635–646.

Brivio, P., Colombo, R., Maggi, M., and Tomasoni, R. (2002). Integration of remote sensing data and GIS for accurate mapping of flooded areas. *International Journal of Remote Sensing*, 23(3):429–441.

Butts, M. B., Payne, J. T., Kristensen, M., and Madsen, H. (2004). An evaluation of the impact of model structure on hydrological modelling uncertainty for streamflow simulation. *Journal of Hydrology*, 298(1):242–266.

Carabajal, C. C. and Harding, D. J. (2006). SRTM C-band and ICESat laser altimetry elevation comparisons as a function of tree cover and relief. *Photogrammetric Engineering & Remote Sensing*, 72(3):287–298.

Casas, A., Benito, G., Thorndycraft, V., and Rico, M. (2006). The topographic data source of digital terrain models as a key element in the accuracy of hydraulic flood modelling. *Earth Surface Processes and Landforms*, 31(4):444–456.

Castro Gama, M., Popescu, I., Mynett, A., Shengyang, L., and van Dam, A. (2013). Modelling extreme flood hazard events on the middle Yellow River using DFLOW-flexible mesh approach. *Natural Hazards and Earth System Sciences Discussions*, 1(6):6061–6092.

Chen, J. L., Wilson, C. R., and Tapley, B. D. (2010). The 2009 exceptional Amazon flood and interannual terrestrial water storage change observed by GRACE. *Water Resources Research*, 46(12).

Coe, M. T., Costa, M. H., Botta, A., and Birkett, C. (2002). Long-term simulations of discharge and floods in the Amazon Basin. *Journal of Geophysical Research: Atmospheres*, 107(D20).

Coe, M. T., Costa, M. H., and Howard, E. A. (2008). Simulating the surface waters of the Amazon River basin: impacts of new river geomorphic and flow parameterizations. *Hydrological processes*, 22(14):2542–2553.

Cogley, J. (2003). GGHYDRO—Global hydrographic data, release 2.3. Trent Tech. Technical report, Note 2003-1.

Conner, J. T. and Tonina, D. (2014). Effect of cross-section interpolated bathymetry on 2D hydrodynamic model results in a large river. *Earth Surface Processes and Landforms*, 39(4):463–475.

Constantine, J. A., Dunne, T., Ahmed, J., Legleiter, C., and Lazarus, E. D. (2014). Sediment supply as a driver of river meandering and floodplain evolution in the Amazon Basin. *Nature Geoscience*, 7(12):899–903.

Courant, R., Friedrichs, K., and Lewy, H. (1928). Über die partiellen Differenzengleichungen der mathematischen Physik. *Mathematische annalen*, 100(1):32–74.

de Graaf, I., Sutanudjaja, E., van Beek, L., and Bierkens, M. (2015). A high-resolution global-scale groundwater model. *Hydrology and Earth System Sciences*, 19(2):823–837.

de Moel, H., Jongman, B., Kreibich, H., Merz, B., Penning-Rowsell, E., and Ward, P. J. (2015). Flood risk assessments at different spatial scales. *Mitigation and Adaptation Strategies for Global Change*, 20(6):865–890.

de Moel, H., van Alphen, J., and Aerts, J. C. J. H. (2009). Flood maps in Europe - methods, availability and use. *Natural Hazards and Earth System Sciences*, 9(2):289–301.

Decharme, B., Alkama, R., Papa, F., Faroux, S., Douville, H., and Prigent, C. (2012). Global off-line evaluation of the ISBA-TRIP flood model. *Climate Dynamics*, 38(7-8):1389–1412.

Deltares (2016). *D-Flow Flexible Mesh User Manual (Draft).* http://oss.deltares.nl/web/delft3dfm/manuals. version 1.1.0, revision 46157.

Dixon, B., Uddameri, V., and Ray, C. (2015). *GIS and Geocomputation for Water Resource Science and Engineering.* John Wiley & Sons.

Falter, D., Dung, N., Vorogushyn, S., Schröter, K., Hundecha, Y., Kreibich, H., Apel, H., Theisselmann, F., and Merz, B. (2016). Continuous, large-scale simulation model for flood risk assessments: proof-of-concept. *Journal of Flood Risk Management*, 9(1):3–21.

Farr, T. G., Rosen, P. A., Caro, E., Crippen, R., Duren, R., Hensley, S., Kobrick, M., Paller, M., Rodriguez, E., Roth, L., et al. (2007). The shuttle radar topography mission. *Reviews of geophysics*, 45(2).

Finaud-Guyot, P., Delenne, C., Guinot, V., and Llovel, C. (2011). 1D–2D coupling for river flow modeling. *Comptes Rendus Mécanique*, 339(4):226–234.

Getirana, A. C., Boone, A., Yamazaki, D., Decharme, B., Papa, F., and Mognard, N. (2012). The hydrological modeling and analysis platform (HyMAP): Evaluation in the Amazon basin. *Journal of Hydrometeorology*, 13(6):1641–1665.

Ghimire, S. (2013). Application of a 2D hydrodynamic model for assessing flood risk from extreme storm events. *Climate*, 1(3):148–162.

Gupta, H. V., Kling, H., Yilmaz, K. K., and Martinez, G. F. (2009). Decomposition of the mean squared error and NSE performance criteria: Implications for improving hydrological modelling. *Journal of Hydrology*, 377(1):80–91.

Guswa, A. J., Brauman, K. A., Brown, C., Hamel, P., Keeler, B. L., and Sayre, S. S. (2014). Ecosystem services: Challenges and opportunities for hydrologic modeling to support decision making. *Water Resources Research*, 50(5):4535–4544.

Hilldale, R. C. and Raff, D. (2008). Assessing the ability of airborne LiDAR to map river bathymetry. *Earth Surface Processes and Landforms*, 33(5):773–783.

Hirabayashi, Y., Mahendran, R., Koirala, S., Konoshima, L., Yamazaki, D., Watanabe, S., Kim, H., and Kanae, S. (2013). Global flood risk under climate change. *Nature Climate Change*, 3(9):816–821.

Hoch, J. M., Haag, A. V., Dam, A. v., Winsemius, H. C., van Beek, L. P., and Bierkens, M. F. (2017a). Assessing the impact of hydrodynamics on large-scale flood wave propagation–a case study for the Amazon Basin. *Hydrology and Earth System Sciences*, 21(1):117–132.

Hoch, J. M., Neal, J. C., Baart, F., van Beek, R., Winsemius, H. C., Bates, P. D., and Bierkens, M. F. (2017b). GLOFRIM v1. 0–A globally applicable computational framework for integrated hydrological–hydrodynamic modelling. *Geoscientific Model Development*, 10(10):3913.

Hollis, G. E. (1975). The effect of urbanization on floods of different recurrence interval. *Water Resources Research*, 11(3):431–435.

Horritt, M. and Bates, P. (2001). Effects of spatial resolution on a raster based model of flood flow. *Journal of Hydrology*, 253(1):239–249.

Horritt, M. and Bates, P. (2002). Evaluation of 1D and 2D numerical models for predicting river flood inundation. *Journal of hydrology*, 268(1):87–99.

Horritt, M., Bates, P., and Mattinson, M. (2006). Effects of mesh resolution and topographic representation in 2D finite volume models of shallow water fluvial flow. *Journal of Hydrology*, 329(1):306–314.

Jongman, B., Hochrainer-Stigler, S., Feyen, L., Aerts, J. C., Mechler, R., Botzen, W. W., Bouwer, L. M., Pflug, G., Rojas, R., and Ward, P. J. (2014). Increasing stress on disaster-risk finance due to large floods. *Nature Climate Change*, 4(4):264–268.

Jonkman, S. N. (2005). Global perspectives on loss of human life caused by floods. *Natural hazards*, 34(2):151–175.

Kernkamp, H. W., Van Dam, A., Stelling, G. S., and de Goede, E. D. (2011). Efficient scheme for the shallow water equations on unstructured grids with application to the Continental Shelf. *Ocean Dynamics*, 61(8):1175–1188.

Kim, J., Warnock, A., Ivanov, V. Y., and Katopodes, N. D. (2012). Coupled modeling of hydrologic and hydrodynamic processes including overland and channel flow. *Advances in Water Resources*, 37:104–126.

Kosuth, P., Callède, J., Laraque, A., Filizola, N., Guyot, J. L., Seyler, P., Fritsch, J. M., and Guimaraes, V. (2009). Sea-tide effects on flows in the lower reaches of the Amazon River. *Hydrological Processes*, 23(22):3141–3150.

Kosuth, P., Larque, A., Soussa da Silva, M., and Filizola, N. (2003). Downstream Amazon river dynamics under oceanic tide influence. In *EGS-AGU-EUG Joint Assembly*.

Kramer, S. C. and Stelling, G. S. (2008). A conservative unstructured scheme for rapidly varied flows. *International journal for numerical methods in fluids*, 58(2):183–212.

Kron, W. (2005). Flood risk= hazard• values• vulnerability. *Water International*, 30(1):58–68.

LeFavour, G. and Alsdorf, D. (2005). Water slope and discharge in the Amazon River estimated using the shuttle radar topography mission digital elevation model. *Geophysical Research Letters*, 32(17).

Legleiter, C. J. and Kyriakidis, P. C. (2008). Spatial prediction of river channel topography by kriging. *Earth Surface Processes and Landforms*, 33(6):841–867.

Legleiter, C. J. and Roberts, D. A. (2009). A forward image model for passive optical remote sensing of river bathymetry. *Remote Sensing of Environment*, 113(5):1025–1045.

Leopold, L. B. and Maddock, T. (1953). *The hydraulic geometry of stream channels and some physiographic implications*, volume 252. US Government Printing Office. 56 pp.

Liang, X., Lettenmaier, D. P., Wood, E. F., and Burges, S. J. (1994). A simple hydrologically based model of land surface water and energy fluxes for general circulation models. *Journal of Geophysical Research: Atmospheres*, 99(D7):14415–14428.

Marengo, J., Nobre, C., Sampaio, G., Salazar, L., and Borma, L. (2011). Climate change in the Amazon Basin: Tipping points, changes in extremes, and impacts on natural and human systems. In *Tropical Rainforest Responses to Climatic Change*, pages 259–283. Springer.

Marengo, J. A. and Espinoza, J. (2016). Extreme seasonal droughts and floods in Amazonia: causes, trends and impacts. *International Journal of Climatology*, 36(3):1033–1050.

Mason, D. C., Cobby, D. M., Horritt, M. S., and Bates, P. D. (2003). Floodplain friction parameterization in two-dimensional river flood models using vegetation heights derived from airborne scanning laser altimetry. *Hydrological processes*, 17(9):1711–1732.

Mason, D. C., J-p. Schumann, G., and Bates, P. D. (2010). *Data Utilization in Flood Inundation Modelling*, pages 209–233. Wiley-Blackwell.

Meade, R. H., Rayol, J. M., Da Conceicão, S. C., and Natividade, J. R. (1991). Backwater effects in the Amazon River basin of Brazil. *Environmental Geology*, 18(2):105–114.

Merwade, V. (2009). Effect of spatial trends on interpolation of river bathymetry. *Journal of Hydrology*, 371(1):169–181.

Merwade, V., Cook, A., and Coonrod, J. (2008). GIS techniques for creating river terrain models for hydrodynamic modeling and flood inundation mapping. *Environmental Modelling & Software*, 23(10):1300–1311.

Moody, J. A. and Troutman, B. M. (2002). Characterization of the spatial variability of channel morphology. *Earth Surface Processes and Landforms*, 27(12):1251–1266.

Muis, S., Verlaan, M., Winsemius, H. C., Aerts, J. C., and Ward, P. J. (2016). A global reanalysis of storm surges and extreme sea levels. *Nature communications*, 7.

Neal, J., Schumann, G., and Bates, P. (2012). A subgrid channel model for simulating river hydraulics and floodplain inundation over large and data sparse areas. *Water Resources Research*, 48(11).

O'Callaghan, J. F. and Mark, D. M. (1984). The extraction of drainage networks from digital elevation data. *Computer vision, graphics, and image processing*, 28(3):323–344.

Paiva, R. C., Buarque, D. C., Clarke, R. T., Collischonn, W., and Allasia, D. G. (2011a). Reduced precipitation over large water bodies in the Brazilian Amazon shown from TRMM data. *Geophysical Research Letters*, 38(4).

Paiva, R. C., Buarque, D. C., Collischonn, W., Bonnet, M.-P., Frappart, F., Calmant, S., and Bulhões Mendes, C. A. (2013a). Large-scale hydrologic and hydrodynamic modeling of the Amazon River basin. *Water Resources Research*, 49(3):1226–1243.

Paiva, R. C., Collischonn, W., and Buarque, D. C. (2013b). Validation of a full hydrodynamic model for large-scale hydrologic modelling in the Amazon. *Hydrological Processes*, 27(3):333–346.

Paiva, R. C., Collischonn, W., and Tucci, C. E. (2011b). Large scale hydrologic and hydrodynamic modeling using limited data and a GIS based approach. *Journal of Hydrology*, 406(3–4):170–181.

Pappenberger, F., Matgen, P., Beven, K. J., Henry, J.-B., Pfister, L., and Fraipont, P. (2006). Influence of uncertain boundary conditions and model structure on flood inundation predictions. *Advances in Water Resources*, 29(10):1430–1449.

Pattison, I., Lane, S. N., Hardy, R. J., and Reaney, S. M. (2014). The role of tributary relative timing and sequencing in controlling large floods. *Water Resources Research*, 50(7):5444–5458.

Pavelsky, T. M. and Smith, L. C. (2008). RivWidth: A software tool for the calculation of river widths from remotely sensed imagery. *IEEE Geoscience and Remote Sensing Letters*, 5(1):70–73.

Paz, A. R. d., Collischonn, W., Tucci, C. E., and Padovani, C. R. (2011). Large-scale modelling of channel flow and floodplain inundation dynamics and its application to the Pantanal (Brazil). *Hydrological processes*, 25(9):1498–1516.

Pekel, J.-F., Cottam, A., Gorelick, N., and Belward, A. S. (2016). High-resolution mapping of global surface water and its long-term changes. *Nature*, 540(7633):418–422.

Poggio, L. and Soille, P. (2012). Influence of pit removal methods on river network position. *Hydrological Processes*, 26(13):1984–1990.

Rennó, C. D., Nobre, A. D., Cuartas, L. A., Soares, J. V., Hodnett, M. G., Tomasella, J., and Waterloo, M. J. (2008). HAND, a new terrain descriptor using SRTM-DEM: Mapping terra-firme rainforest environments in Amazonia. *Remote Sensing of Environment*, 112(9):3469–3481.

Rinaldo, A., Marani, A., and Rigon, R. (1991). Geomorphological dispersion. *Water Resources Research*, 27(4):513–525.

Rodríguez, E., Morris, C., Belz, J., Chapin, E., Martin, J., Daffer, W., and Hensley, S. (2005). An assessment of the SRTM topographic products. Technical report, Technical Report JPL D-31639, Jet Propulsion Laboratory, Pasadena, California.

Rodríguez-Iturbe, I. and Valdes, J. B. (1979). The geomorphologic structure of hydrologic response. *Water resources research*, 15(6):1409–1420.

Rudorff, C. M., Melack, J. M., and Bates, P. D. (2014). Flooding dynamics on the lower Amazon floodplain: 1. Hydraulic controls on water elevation, inundation extent, and river-floodplain discharge. *Water Resources Research*, 50(1):619–634.

Saco, P. and Kumar, P. (2004). Kinematic dispersion effects of hillslope velocities. *Water resources research*, 40(1).

Salati, E. and Marques, J. (1984). Climatology of the Amazon region. In *The Amazon*, pages 85–126. Springer.

Salati, E. and Vose, P. B. (1984). Amazon basin: a system in equilibrium. *Science*, 225:129–139.

Savage, J. T. S., Bates, P., Freer, J., Neal, J., and Aronica, G. (2016). When does spatial resolution become spurious in probabilistic flood inundation predictions? *Hydrological Processes*, 30(13):2014–2032.

Schumann, G., Matgen, P., Cutler, M., Black, A., Hoffmann, L., and Pfister, L. (2008). Comparison of remotely sensed water stages from LiDAR, topographic contours and SRTM. *ISPRS Journal of Photogrammetry and Remote Sensing*, 63(3):283–296.

Schumann, G. J.-P., Moller, D. K., and Mentgen, F. (2016). High-accuracy elevation data at large scales from airborne single-pass SAR interferometry. *Frontiers in Earth Science*, 3:88.

Schumann, G.-P., Neal, J. C., Voisin, N., Andreadis, K. M., Pappenberger, F., Phanthuwongpakdee, N., Hall, A. C., and Bates, P. D. (2013). A first large-scale flood inundation forecasting model. *Water Resources Research*, 49(10):6248–6257.

Sioli, H. (1984). The Amazon and its main affluents: hydrography, morphology of the river courses, and river types. In *The Amazon*, pages 127–165. Springer.

Smith, M. J., Edwards, E. P., Priestnall, G., and Bates, P. (2006). Exploitation of new data types to create digital surface models for flood inundation modeling. *FRMRC Research Rep. UR3.* 25 pp.

Stelling, G. S. and Duinmeijer, S. A. (2003). A staggered conservative scheme for every Froude number in rapidly varied shallow water flows. *International journal for numerical methods in fluids*, 43(12):1329–1354.

Sutanudjaja, E., van Beek, L., de Jong, S., van Geer, F., and Bierkens, M. (2014). Calibrating a large-extent high-resolution coupled groundwater-land surface model using soil moisture and discharge data. *Water Resources Research*, 50(1):687–705.

Tarboton, D. G., Bras, R. L., and Rodriguez-Iturbe, I. (1991). On the extraction of channel networks from digital elevation data. *Hydrological processes*, 5(1):81–100.

Teng, J., Jakeman, A., Vaze, J., Croke, B., Dutta, D., and Kim, S. (2017). Flood inundation modelling: A review of methods, recent advances and uncertainty analysis. *Environmental Modelling & Software*, 90(Supplement C):201 – 216.

Trigg, M. A., Bates, P. D., Wilson, M. D., Schumann, G., and Baugh, C. (2012). Floodplain channel morphology and networks of the middle Amazon River. *Water Resources Research*, 48(10).

Trigg, M. A., Wilson, M. D., Bates, P. D., Horritt, M. S., Alsdorf, D. E., Forsberg, B. R., and Vega, M. C. (2009). Amazon flood wave hydraulics. *Journal of Hydrology*, 374(1):92–105.

van Beek, L., Wada, Y., and Bierkens, M. F. (2011). Global monthly water stress: 1. Water balance and water availability. *Water Resources Research*, 47(7).

van Beek, L. P. H. and Bierkens, M. F. P. (2009). The global hydrological model PCR-GLOBWB: conceptualization, parameterization and verification. Technical report, Department of Physical Geography, Utrecht University, The Netherlands.

van Beek, L. P. H., Eikelboom, T., Vliet, M. T., and Bierkens, M. F. (2012). A physically based model of global freshwater surface temperature. *Water Resources Research*, 48(9).

Wada, Y., Flörke, M., Hanasaki, N., Eisner, S., Fischer, G., Tramberend, S., Satoh, Y., van Vliet, M., Yillia, P., Ringler, C., et al. (2016). Modeling global water use for the 21st century: Water Futures and Solutions (WFaS) initiative and its approaches. *Geoscientific Model Development*, 9:175–222.

Wada, Y., van Beek, L. P. H., van Kempen, C. M., Reckman, J. W., Vasak, S., and Bierkens, M. F. (2010). Global depletion of groundwater resources. *Geophysical research letters*, 37(20).

Wada, Y., Wisser, D., and Bierkens, M. (2014). Global modeling of withdrawal, allocation and consumptive use of surface water and groundwater resources. *Earth System Dynamics*, 5(1):15.

Weedon, G. P., Balsamo, G., Bellouin, N., Gomes, S., Best, M. J., and Viterbo, P. (2014). The WFDEI meteorological forcing data set: WATCH Forcing Data methodology applied to ERA-Interim reanalysis data. *Water Resources Research*, 50(9):7505–7514.

Werner, M., Hunter, N., and Bates, P. (2005). Identifiability of distributed floodplain roughness values in flood extent estimation. *Journal of Hydrology*, 314(1):139–157.

Wesseling, C. G., Karssenberg, D., Burrough, P. A., and van Deursen, W. P. A. (1996). Integrating dynamic environmental models in GIS: the development of a Dynamic Modelling language. *Transactions in GIS*, 1(1):40–48.

Wilson, M., Bates, P., Alsdorf, D., Forsberg, B., Horritt, M., Melack, J., Frappart, F., and Famiglietti, J. (2007). Modeling large-scale inundation of Amazonian seasonally flooded wetlands. *Geophysical Research Letters*, 34(15).

Winsemius, H., van Beek, L., Jongman, B., Ward, P., and Bouwman, A. (2013). A framework for global river flood risk assessments. *Hydrology and Earth System Sciences*, 17(5):1871–1892.

Yamazaki, D., Baugh, C. A., Bates, P. D., Kanae, S., Alsdorf, D. E., and Oki, T. (2012a). Adjustment of a spaceborne DEM for use in floodplain hydrodynamic modeling. *Journal of Hydrology*, 436:81–91.

Yamazaki, D., Ikeshima, D., Tawatari, R., Yamaguchi, T., O'Loughlin, F., Neal, J. C., Sampson, C. C., Kanae, S., and Bates, P. D. (2017). A high accuracy map of global terrain elevations. *Geophysical Research Letters*.

Yamazaki, D., Kanae, S., Kim, H., and Oki, T. (2011). A physically based description of floodplain inundation dynamics in a global river routing model. *Water Resources Research*, 47(4).

Yamazaki, D., Lee, H., Alsdorf, D. E., Dutra, E., Kim, H., Kanae, S., and Oki, T. (2012b). Analysis of the water level dynamics simulated by a global river model: A case study in the Amazon River. *Water Resources Research*, 48(9).

Yamazaki, D., O'Loughlin, F., Trigg, M. A., Miller, Z. F., Pavelsky, T. M., and Bates, P. D. (2014a). Development of the global width database for large rivers. *Water Resources Research*, 50(4):3467–3480.

Yamazaki, D., Sato, T., Kanae, S., Hirabayashi, Y., and Bates, P. D. (2014b). Regional flood dynamics in a bifurcating mega delta simulated in a global river model. *Geophysical Research Letters*, 41(9):3127–3135.

Yan, K., Di Baldassarre, G., and Solomatine, D. P. (2013). Exploring the potential of SRTM topographic data for flood inundation modelling under uncertainty. *Journal of hydroinformatics*, 15(3):849–861.

Zhao, G.-j., Gao, J.-f., Tian, P., and Tian, K. (2009). Comparison of two different methods for determining flow direction in catchment hydrological modeling. *Water Science and Engineering*, 2(4):1–15.

Appendix A

Accounting for lakes in PS YG and PS YP (Chapter 4.2.4.2.2.3)

Table A.1 shows the original and adjusted (averaged) riverbed elevations in PS YG and PS YP. Only sample points exhibiting river widths larger than 8,000 m were inspected with OpenStreetMap and its riverbed elevations altered in case they represented lakes.

Table A.1: Original and adjusted riverbed elevation values (in meters) in PS YG and PS YP.

lon	lat	riverbed elevations			
		PS YG		PS YP	
		original	adjusted	original	adjusted
-54.247	-2.301	-82.6	-36.1	-56.8	-42.2
-54.302	-2.351	-53.1	-36.1	-48.5	-42.2
-54.650	-2.372	-43.7	-28.5	-45.2	-38.3
-54.668	-2.250	-73.4	-28.5	-54.5	-38.3
-54.599	-2.149	-38.7	-28.5	-42.7	-38.3
-54.728	-2.150	-58.1	-28.5	-50.1	-38.3
-54.827	-2.105	-34.7	-28.5	-41.0	-38.3
-54.907	-2.075	-39.9	-28.5	-43.1	-38.3
-54.981	-2.126	-41.0	-28.5	-43.5	-38.3
-55.776	-1.936	-58.3	-28.8	-49.5	-38.3
-55.877	-1.913	-59.2	-28.8	-49.7	-38.3
-56.031	-1.826	-34.4	-17.3	-40.9	-31.1
-56.625	-2.257	-32.7	-10.6	-40.1	-22.8
-55.950	-1.957	-46.3	-28.8	-45.5	-38.3
-56.925	-2.634	-34.5	-21.8	-39.2	-33.3
-57.027	-2.625	-42.7	-21.8	-42.3	-33.3
-59.550	-1.823	6.3	28.4	-2.3	12.6
-59.643	-1.750	-17.7	28.4	-11.3	12.6
-59.739	-1.624	-12.1	28.4	-7.3	12.6
-59.676	-3.146	-36.2	-10.1	-38.0	-25.0
-62.131	-4.427	-22.9	-2.4	-29.7	-17.9
-55.250	-2.204	-33.2	-34.6	-40.4	-41.0
-55.376	-2.211	-51.2	-34.6	-47.2	-41.0
-55.526	-2.141	-29.8	-34.6	-38.8	-41.0
-55.650	-2.144	-35.2	-34.6	-41.2	-41.0

Appendix B

Results - Accuracy Analysis (Chapter 5.3)

B.1 Discharge at Obidos (Chapter 5.3.1)

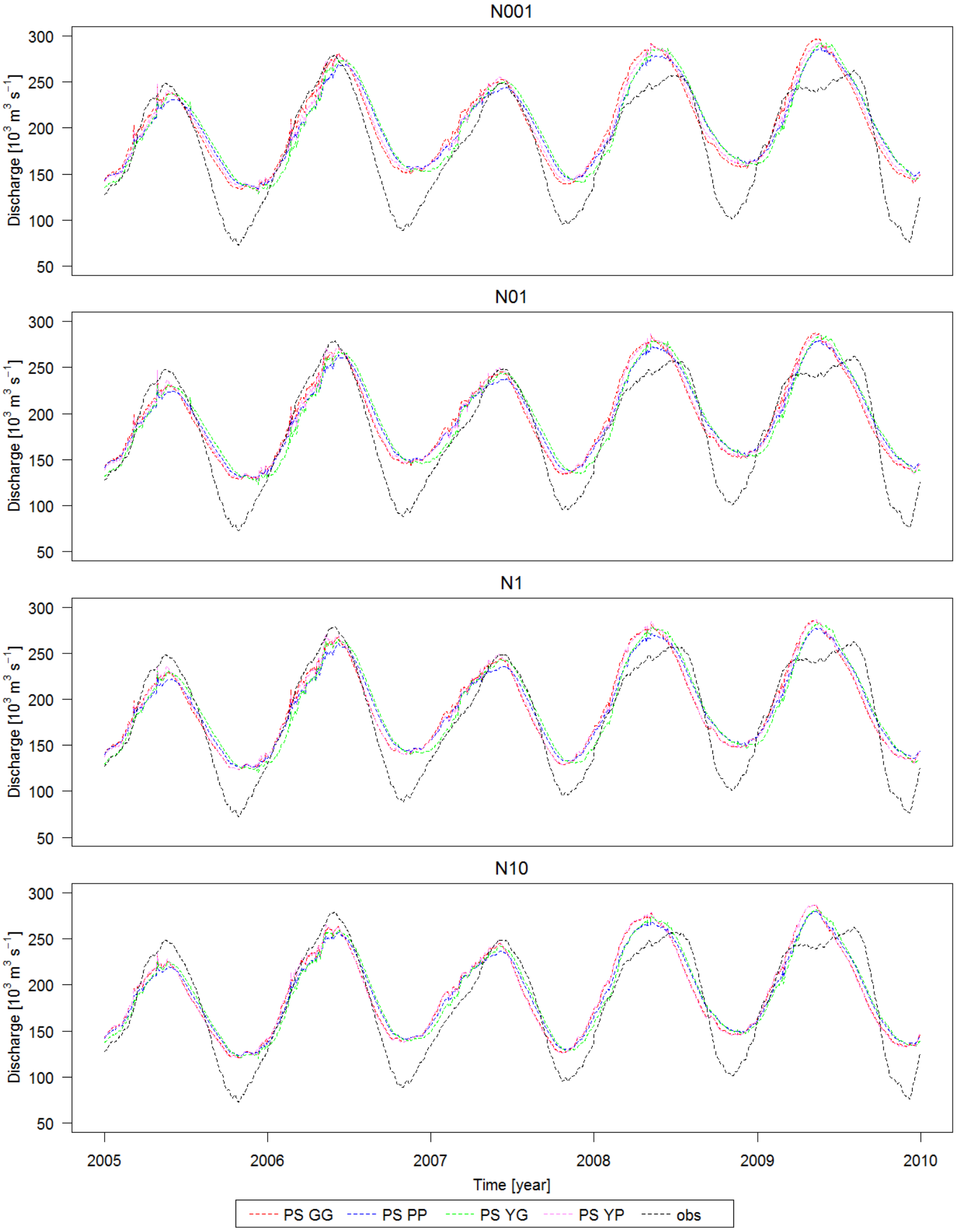

Figure B.1: Observed and simulated discharge at Obidos.

B.2 Normalized water level at Obidos (Chapter 5.3.2)

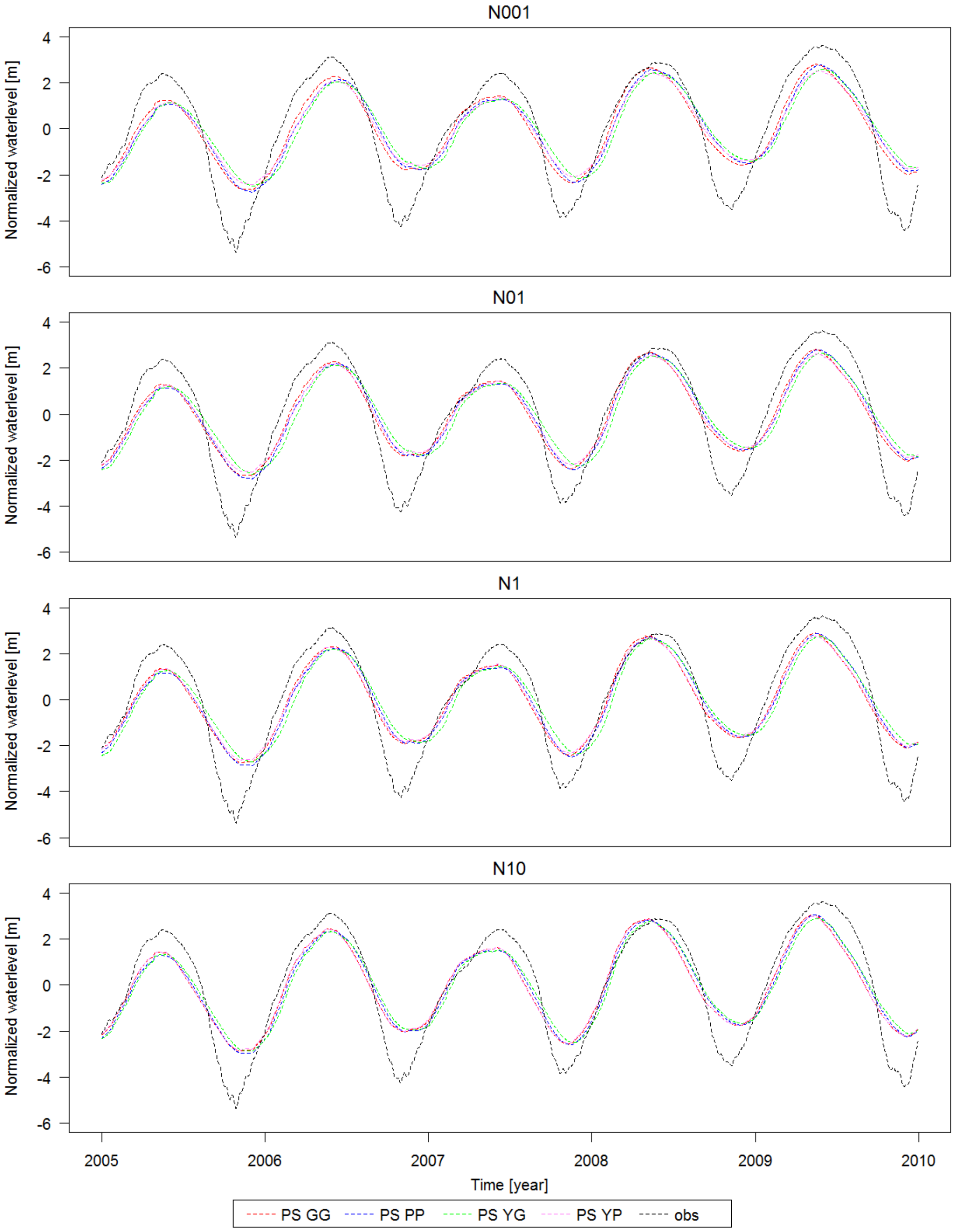

Figure B.2: Observed and simulated normalized water levels at Obidos.